






# Snow Depth and Snow Water Equivalent Estimation in the Northwestern Himalayan Watershed using Spaceborne Polarimetric SAR Interferometry

 Sayantan Majumdar<sup>a,b,\*</sup>,  Praveen K. Thakur<sup>b</sup>,  Ling Chang<sup>a</sup>,  
 Sneh Mani<sup>c</sup>,  Shashi Kumar<sup>b</sup>

<sup>a</sup>*Faculty of Geo-information Science and Earth Observation (ITC), University of Twente*

<sup>b</sup>*Indian Institute of Remote Sensing (IIRS), ISRO*

<sup>c</sup>*Snow and Avalanche Study Establishment (SASE), DRDO*

---


## Abstract

Snow depth (SD) and Snow Water Equivalent (SWE) constitute essential physical properties of snow and find extensive usage in the hydrological modelling domain. However, the prominent impact of the hydrometeorological conditions and difficult terrain conditions inhibit accurate measurement of the SD and SWE— an ongoing research problem in the cryosphere paradigm. In this context, spaceborne synthetic aperture radar (SAR) systems benefit from global coverage at sufficiently high spatial and temporal resolutions. Still, existing polarimetric and interferometric SAR techniques are susceptible to high volume scattering resulting from the increased snow grain sizes due to the standing (or old) snow formation driven by the temperature induced snow metamorphosis process. Hence, to model this volume decorrelation, the polarimetric SAR interferometry (Pol-InSAR) technique can be effectively applied. In this work, the standing snow depth (SSD) and its corresponding standing snow water equivalent (SSWE) are estimated using the single-baseline Pol-InSAR based hybrid Digital Elevation Model (DEM) differencing and coherence amplitude inversion model. To achieve this, six TerraSAR-X, TanDEM-X Coregistered Single look Slant range Complex (CoSSC) bistatic quad-pol acquisitions between December 2015 and January 2016 over Dhundi (situated in the Beas watershed, northwestern Himalayas, India) are used. Due to the associated problems of model parameter tuning, complex topographical conditions, and limited ground-truth measurements, appropriate sensitivity analyses have been carried out for the parameter optimisation. Furthermore, the uncertainty sources are identified by performing a summer (June 8, 2017) and wintertime (January 8, 2016) comparative analysis of the study area which quantitatively highlights the changes in the percentages of the surface and volume scatterings. Evidently, the improved model displays sufficiently high overall SSD accuracy with coefficient of determination ( $R^2$ )  $\approx$  0.96, Mean Absolute Error (MAE)  $\approx$  1.61 cm, and Root Mean Square Error (RMSE)  $\approx$  2.16 cm. Additionally, the respective SSWEs have been calculated by assuming a fixed snow density for each epoch wherein the overall error metrics are  $R^2 \approx$  0.71, MAE  $\approx$  5.19 mm, and RMSE  $\approx$  6.84 mm. Therefore, this research successfully demonstrates the practicability of the improved Pol-InSAR model for SD estimation over rugged terrains.

*Keywords:* Pol-InSAR, Microwave Remote Sensing, Synthetic Aperture Radar, Polarimetry, Interferometry, Snow Depth, Snow Water Equivalent, Watershed, Sensitivity Analysis

---

\*Corresponding author

Email address: [ir.sayantan.majumdar@gmail.com](mailto:ir.sayantan.majumdar@gmail.com) ( Sayantan Majumdar )

## 1. Introduction

Snow depth (SD) and snow water equivalent (SWE) are two of the most important physical properties of snow and are extensively used in hydrological models that relate to snowmelt runoff and snow avalanche predictions (Thakur et al., 2017). While snow depth or snow height refers to the distance of the ground to the snow surface, SWE quantifies the amount of water present in a snowpack (layered snow formed by accumulation over time). Theoretically, SWE is defined as the product of snow depth and snow density and can be conceptualised as the amount of liquid water obtained owing to the instantaneous melting of an entire snowpack (Tedesco, 2015). Obtaining accurate estimation of the SD and SWE is quite challenging depending upon the data availability, variety, and quality, parameterisation method, mathematical model selection, and the hydrometeorological conditions. Hence, it is considered to be an important research element in the cryosphere paradigm (Leinss et al., 2014, 2015, 2016; Conde et al., 2019).

Due to the difficulties posed by in-situ or ground based measurements of the SD and SWE in rugged terrains, remote sensing techniques coupled with adequately sampled (both in space and time domains) ground measurements are widely used to improve the quality of these estimated parameters over considerably large areas (Takala et al., 2011). Currently, LiDAR (Light Detection and Ranging) and spaceborne SAR (Synthetic Aperture Radar) are the most popular techniques used in the studies related to snow, ice and the cryosphere in general (Deems et al., 2013; Leinss et al., 2014; Tedesco, 2015). However, LiDAR can only be used to determine the height of the snow and cannot be used for measuring other physical properties such as snow density and snow wetness (Tedesco, 2015; Leinss et al., 2014). In addition, the operating cost of LiDAR is sufficiently high and is also weather dependent (Deems et al., 2013). As a result, spaceborne SAR systems benefit from substantial coverage (globally available), cloud insensitivity, all-day operability and are extensively used to measure the snow physical properties sufficiently at high spatial resolutions (Moreira et al., 2013; Thakur et al., 2012).

The applicability of SAR systems for snow cover monitoring was discussed as early as 1977 (Ulaby et al., 1977) wherein the snow backscatter coefficient was measured and was thereafter modelled for various frequencies, layers, and polarisations (Zuniga et al., 1979). It was shown that only very high microwave frequencies (Ku-band or higher) exhibit a significant dependence on SD or the SWE of dry or standing (deposited) snow (Yueh et al., 2009). However, lower frequencies (X-band or below) penetrate through dry snow whereby the underneath frozen soil or ground primarily contributes to the radar backscatter signal. Whereas, in case of moist snow (the transitional stage between dry and wet snow) and wet snow, the predominant scattering occurs from the snow volume and snow surface respectively due to the presence of water. Essentially, water, with its high dielectric constant, heavily modifies the dielectric properties of snow and effectively reduces the snow penetration capacity of the radar pulses (Abe et al., 1990). The radar backscattering mechanism for a typical snow covered area can be conceptualised from Figure 1.1. In principle, Polarimetric SAR (PolSAR) and Interferometric SAR (InSAR) techniques utilise these received target echoes to support various microwave remote sensing applications in the cryosphere domain.

PolSAR based algorithms which work on the polarimetric backscatter signal have been widely adopted for various snow related applications such as the classification of dry and

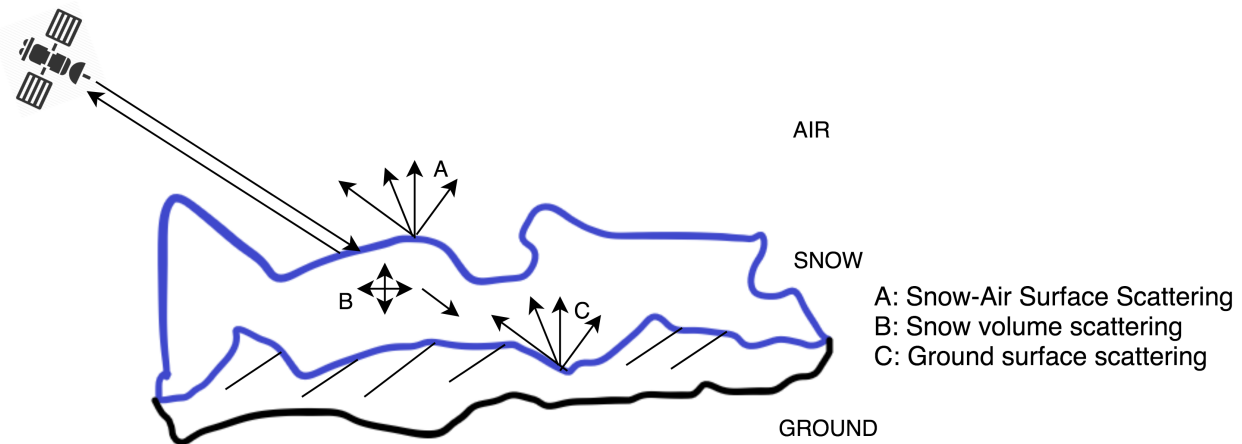


Figure 1.1: Conceptual diagram displaying the radar backscattering mechanism in hilly terrains. Adapted from [Thakur et al. \(2012\)](#).

82 wet snow, measuring snow wetness and snow density ([Singh et al., 2017](#); [Snehmani et al.,](#)  
 83 [2010](#); [Thakur et al., 2012, 2017](#); [Usami et al., 2016](#)). [Leinss et al. \(2014\)](#) introduced the use  
 84 of spaceborne PolSAR for snow height determination, wherein the relationship between the  
 85 copolar phase difference (CPD) and fresh snow depth is quantitatively analysed by deriving  
 86 a theoretical model. Moreover, InSAR techniques find significant usage in the cryosphere  
 87 domain and have been used to measure dry snow depth and SWE in several studies ([Conde](#)  
 88 [et al., 2019](#); [Gneriussen et al., 2001](#); [Leinss et al., 2015](#); [Li et al., 2017](#); [Liu et al., 2017](#)). In  
 89 this context, the Pol-InSAR technique works on the coherent combination of both PolSAR  
 90 and InSAR observations, thereby enabling the interferogram generation in arbitrary transmit  
 91 and receive channels ([Papathanassiou & Cloude, 2001](#); [Cloude, 2005, 2010](#)). It has been  
 92 widely used for estimating tree height in forested regions and can be effectively applied to  
 93 natural or artificial volume scatterers including snow and ice ([Leinss et al., 2014](#); [Hajnsek](#)  
 94 [et al., 2009](#); [Kugler et al., 2015](#); [Kumar et al., 2017](#); [Papathanassiou & Cloude, 2001](#)).

95 The prime focus of this research is to estimate the standing snow depth (SSD) using the  
 96 Pol-InSAR technique. Additionally, the corresponding standing SWE (SSWE) is calculated  
 97 based on a fixed snow density. In this work, the main innovation lies in improving  
 98 the Pol-InSAR based hybrid DEM differencing and coherence amplitude inversion model  
 99 ([Cloude, 2005, 2010](#); [Majumdar et al., 2019b](#)). This model is successfully tested for six fully  
 100 polarimetric (quad-pol) TerraSAR-X/TanDEM-X ([Balss et al., 2012](#)) data acquired between  
 101 December 2015 and January 2016 over Dhundi, situated in the Beas river watershed of the  
 102 northwestern Himalayas near Manali. The results are obtained after performing thorough  
 103 sensitivity analysis of the free model parameters. Furthermore, the scattering characteristics  
 104 of the study area are analysed using the dual-pol entropy ( $H$ ) and scattering angle ( $\alpha$ )  
 105 or  $H/\alpha$  decomposition, and unsupervised Wishart classification techniques ([Lee & Pottier,](#)  
 106 [2009](#); [Cloude, 2010](#); [Singh et al., 2014](#)) for identifying the potential uncertainty sources.

107 This manuscript is organised in five primary sections and starts with an introductory  
 108 discussion in section 1. Thereafter, the technical workflow is described in section 2 following  
 109 which the study area including required datasets and software are specified (section 3).  
 110 Finally, the results (section 4) and the relevant conclusions (section 5) are put forward.

## 111 2. Methodology

112 This section deals with the methodological framework which has been followed to generate  
113 the SSD and SSWE results. The pre-processing steps are briefly discussed in section 2.1 and  
114 the Pol-InSAR based approach used for the SSD estimation is addressed in section 2.2.  
115 Moreover, the uncertainty assessment, validation and sensitivity analysis tasks are described  
116 in section 2.3.

### 117 2.1. Data Preprocessing

118 Since the SAR datasets are already coregistered, separate coregistration step has not  
119 been performed. For the SSD inversion model, the geocoded or terrain-corrected data (3 m  
120 spatial resolution) consists of the quad-pol channels, HH, HV, VH, and VV. Additionally,  
121 the local incidence angle (LIA) is computed from the ALOS PALSAR DEM (Fig 3.1).  
122 It should be noted that, for the Pol-InSAR technique, processing both the TanDEM-X  
123 (master) and TerraSAR-X (slave) images (Balss et al., 2012) are mandatory for generating  
124 the interferogram. The dataset descriptions are provided in section 3.2.

### 125 2.2. Pol-InSAR based Standing Snow Depth Estimation

126 Standing or old snow refers to the deposited snow on the ground which has accumulated  
127 over time (Reynolds, 1983; Majumdar et al., 2019b). Typically, old snow due to the presence  
128 of impurity and temperature-gradient induced recrystallisation process consists of snow  
129 particles larger than the X-band microwave wavelengths and results in volume scattering  
130 (Leinss et al., 2016; Riche et al., 2013). This volume decorrelation can be quantitatively  
131 analysed with the help of the Pol-InSAR technique (Cloude, 2010) to obtain the volumetric  
132 SSD ( $\Delta Z_s$ ).

#### 133 2.2.1. Single-baseline Pol-InSAR Specifics

134 The single baseline Pol-InSAR algorithm works on the basis of the complex coherence,  
135  $\tilde{\gamma}(\vec{w}_1, \vec{w}_2)$ , defined in Eq. (2.1a) where  $I_i(\vec{w}_1, \vec{w}_2)$  denotes the  $i^{\text{th}}$  pixel coordinate value of  
136 the wrapped Pol-InSAR interferogram,  $I(\vec{w}_1, \vec{w}_2)$  obtained in Eq. (2.1b). This interferogram  
137 is calculated from Eq. (2.1c) and Eq. (2.1d) where the coregistered master ( $s_1$ ) and slave  
138 ( $s_2$ ) images are acquired at a given polarisation vector,  $(\vec{w})$  respectively. Here, the weight  
139 vectors,  $\vec{w}_1$  and  $\vec{w}_2$  are selected by the user based on the scattering mechanisms at ends 1  
140 and 2 of the interferometric baseline. If  $\vec{w}_1 = \vec{w}_2$ ,  $\tilde{\gamma}(\vec{w}_1, \vec{w}_2)$  can be alternatively specified as  
141  $\tilde{\gamma}(\vec{w}_1)$  (Cloude, 2005, 2010). Moreover,  $L$  is the total number of pixels averaged in the range  
142 and azimuth directions which can be replaced by the ensemble averaging operation following  
143 the statistical ergodicity assumption (Hanssen, 2001; Hoen & Zebker, 2000; Kugler et al.,  
144 2015; Kumar et al., 2017; Papathanassiou & Cloude, 2001). Additionally,  $\phi_{flat}^w \in [0, 2\pi)$  is  
145 the wrapped flat-earth phase obtained from the estimated absolute flat-earth phase,  $\phi_{flat}$   
146 and has to be removed from  $I(\vec{w}_1, \vec{w}_2)$  as shown in Eq. (2.1b). Also, the calculation of the

147 generalised weight vector,  $\vec{w}$  is given by Eq. (2.1e).

$$\tilde{\gamma}(\vec{w}_1, \vec{w}_2) = \frac{\sum_{i=1}^L I_i(\vec{w}_1, \vec{w}_2)}{\sqrt{\sum_{i=1}^L |s_{1i}(\vec{w}_1)|^2 \sum_{i=1}^L |s_{2i}(\vec{w}_2)|^2}}, |\tilde{\gamma}(\vec{w}_1, \vec{w}_2)| \in [0, 1] \quad (2.1a)$$

$$I(\vec{w}_1, \vec{w}_2) = s_1(\vec{w}_2) s_2^*(\vec{w}_2) e^{-j\phi_{flat}} \quad (2.1b)$$

$$s_1 = w_1^1 \frac{s_{hh}^1 + s_{vv}^1}{\sqrt{2}} + w_1^2 \frac{s_{hh}^1 - s_{vv}^1}{\sqrt{2}} + w_1^3 \sqrt{2} s_{hv}^1 \quad (2.1c)$$

$$s_2 = w_2^1 \frac{s_{hh}^2 + s_{vv}^2}{\sqrt{2}} + w_2^2 \frac{s_{hh}^2 - s_{vv}^2}{\sqrt{2}} + w_2^3 \sqrt{2} s_{hv}^2 \quad (2.1d)$$

$$\vec{w} = [w^1 \quad w^2 \quad w^3]^T = [\cos \alpha \quad \sin \alpha \cos \beta e^{j\delta} \quad \sin \alpha \sin \beta e^{j\mu}]^T \quad (2.1e)$$

148 where,  $s_{pp}^1$  and  $s_{pp}^2$  correspond to the master (1) and slave (2) images respectively,  $pp \in$   
 149  $\{hh, hv, vv\}$ , and  $*$  denotes the complex conjugate operator.

150 In this case, the parameters, scattering angle ( $\alpha$ ), target orientation angle ( $\beta$ ), phase  
 151 terms ( $\delta$  and  $\mu$ ), are chosen according to the selected polarisation given by Table 2.1. LL,  
 152 LR and RR correspond to the left circular, left-right circular and right circular polarisations  
 153 (Cloude, 2010). However, it is possible to optimise these parameters specific to the data, the  
 154 details of which are provided by Cloude (2010).

Table 2.1: Pol-InSAR scattering mechanisms (Cloude, 2005).

Polarisation Selection	$\alpha(^{\circ})$	$\beta(^{\circ})$	$\delta(^{\circ})$	$\mu(^{\circ})$
HH	45	0	0	0
HV	90	90	0	0
VV	45	180	0	0
HH+VV	0	0	0	0
HH-VV	90	0	0	0
LL	90	45	0	90
LR	0	0	0	0
RR	90	45	0	-90

### 155 2.2.2. Height Inversion Algorithm Details

156 In this study, the modified (also improved) hybrid DEM differencing and coherence  
 157 amplitude based Pol-InSAR volumetric height inversion model as given by Eq. (2.2a) is  
 158 used for the SSD estimation (Majumdar et al., 2019b). The sensitivity analyses for these  
 159 parameters are discussed in section 4.3. Accordingly, the parameter values which are specified  
 160 in this section represent those for the best fit model.

161 Firstly, the volume scattering dominant channels, HV and VH, are averaged to fully  
 162 utilise the quad-pol data (Cloude, 2005). Next, the Pol-InSAR interferogram,  $I(\vec{w}_v)$  has  
 163 been computed using Eq. (2.1b) wherein, the weight vector,  $\vec{w}_v$  is obtained from Table 2.1  
 164 for the HV polarisation. Thereafter, the complex volume coherence,  $\tilde{\gamma}(\vec{w}_v)$ , is calculated  
 165 from Eq. (2.1a) with  $L = 5$ . Similarly, the complex surface or ground coherence,  $\tilde{\gamma}(\vec{w}_s)$ , is

166 computed by choosing  $\vec{w}_s$  as the HH-VV weight vector (Table 2.1). Moreover, the actual  
 167 vertical wavenumber,  $k_z$ , when varied with the LIA, is quite small ( $< 0.3$  rad/m) with the  
 168 ambiguity height,  $h_{2\pi} = 2\pi/k_z > 17$  m,  $\lambda_0 \approx 3.11$  cm and  $m = 1$  (single-pass acquisition).  
 169 Since the maximum height of the distributed volume scatterer (in this case, standing snow),  
 170  $\Delta Z_{s,max}$ , should be similar to  $h_{2\pi}$  (Kugler et al., 2015; Hajnsek et al., 2009; Kumar et al.,  
 171 2017),  $k_z$  has to be rescaled to an optimum range for effectively estimating the SSD. Hence,  
 172 the modified vertical wavenumber,  $k'_z$ , is given by Eq. (2.2b) where  $\eta'$  is a free scaling  
 173 parameter which has to be set according to the known  $\Delta Z_{s,max}$  in the study area. Here,  
 174  $h'_{2\pi}$  is the scaled height of ambiguity which like that of  $h_{2\pi}$  determines the height changes  
 175 in modulo  $2\pi$  (Hanssen, 2001). Also,  $\mathbb{R}_{>0}^+$  denotes the set of all positive real numbers in  
 176 the interval  $(0, \infty)$ . In this work, due to the limited ground-truth data availability and the  
 177 subsequent ensemble averaging operation (window size of  $5 \times 5$ ) on  $k'_z$ ,  $\eta'$  is optimised based  
 178 on the Mean Absolute Error (MAE) of the SSD estimates.

179 Apart from this, the function  $\arg$  is defined in the interval  $[0, 2\pi)$  and the parameter  $m$   
 180 is set to 1 for bistatic acquisition and 2 in the monostatic case. Also in Eq. (2.2b) and  
 181 (2.2c),  $\Delta\theta$  is the change in the incidence angle occurring due to the spatial baseline,  $\theta_l$  is the  
 182 LIA,  $\lambda_0$  is the radar wavelength (Cloude, 2010; Kugler et al., 2015),  $\epsilon_s$  is the real part of the  
 183 dielectric permittivity of the snow volume wherein  $\rho_s$  is the standing snow density (Sharma  
 184 et al., 2007; Leinss et al., 2015).

$$\Delta Z_s = \frac{\arg(\tilde{\gamma}(\vec{w}_v) e^{-j\phi_{topo}^w})}{k'_z} + \eta \frac{\text{sinc}_{\pi}^{-1}(\gamma(\vec{w}_v))}{k'_z}, \eta \in [0, 1] \quad (2.2a)$$

185 where,

$$k'_z = \left\langle \eta' \frac{m \Delta\theta \sqrt{\epsilon_s}}{\lambda_0 \sin \theta_l} \right\rangle, \eta' \in \mathbb{R}_{>0}^+ \mid \Delta Z_{s,max} \approx h'_{2\pi} = 2\pi/k'_z \quad (2.2b)$$

$$\epsilon_s = 1 + 1.5995\rho_s + 1.8610\rho_s^3 \quad (2.2c)$$

186 Subsequently, the volume and surface coherences are then used to estimate the wrapped  
 187 ground phase,  $\phi_{topo}^w \in [0, 2\pi)$ , from Eq. (2.3). Additionally, a median ensemble filter of  $5 \times 5$   
 188 is applied on the obtained  $\phi_{topo}^w$  following the processing steps provided by Cloude (2005).

$$\phi_{topo}^w = \arg(\tilde{\gamma}(\vec{w}_v) - \tilde{\gamma}(\vec{w}_s)(1 - L_{\vec{w}_s})) \quad (2.3)$$

where,

$$L_{\vec{w}_s} = \frac{-B - \sqrt{B^2 - 4AC}}{2A}, L_{\vec{w}_s} \in [0, 1]$$

$$A = |\tilde{\gamma}(\vec{w}_v)|^2 - 1$$

$$B = 2\Re(\tilde{\gamma}(\vec{w}_v) - \tilde{\gamma}(\vec{w}_s)\tilde{\gamma}^*(\vec{w}_v))$$

$$C = |\tilde{\gamma}(\vec{w}_v) - \tilde{\gamma}(\vec{w}_s)|^2$$

189 Eventually, the SSD ( $\Delta Z_s$ ) and SSWE ( $= \rho_s \Delta Z_s$ ) are estimated using the standing snow  
 190 densities given in Table 3.2. Here,  $\eta = 0.6$  is kept fixed and the SSD values are averaged

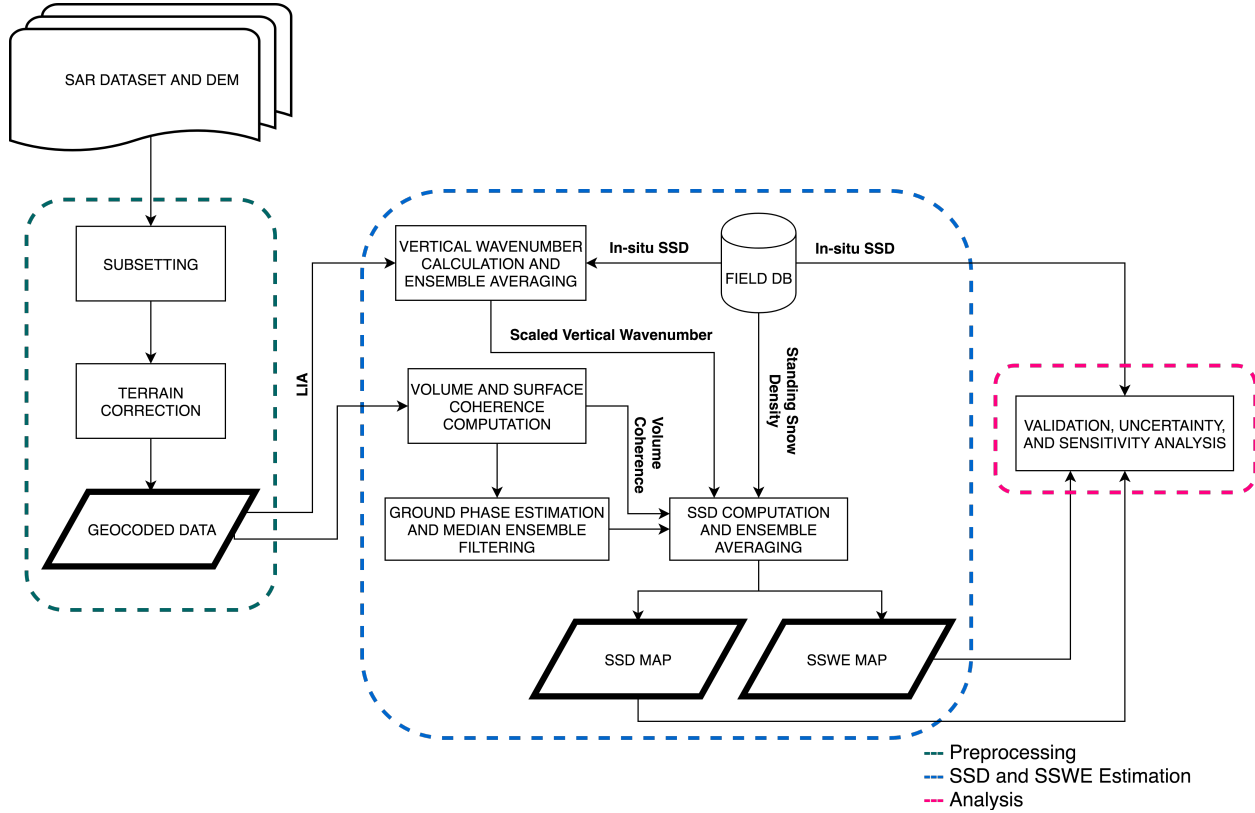


Figure 2.1: SSD and SSWE estimation workflow using Pol-InSAR.

191 based on a  $5 \times 5$  ensemble filter window. The entire Pol-InSAR workflow is summarised in  
 192 Figure 2.1 which shows the main processing blocks.

193 However, in order to compute the inverse  $\text{sinc}_\pi$  (normalised sinc) function in Eq. (2.2a),  
 194 the Cloude (2010) approximation ( $\text{sinc}_C^{-1}$ ) in Eq. (2.4a) is replaced by Eq. (2.4b) where  
 195 the secant method (Cheney & Kincaid, 2012) has been applied to find  $\alpha_r \in \mathbb{R}$  (rad), the  
 196 desired root or inverse. Moreover, to make the Cloude (2010) approximation compliant with  
 197 the scientific computing libraries such as SciPy (Jones et al., 2001) which use the  $\text{sinc}_\pi$   
 198 function, the normalised variant of Eq. (2.4a) given by Eq. (2.4c) is incorporated where  
 199  $\text{sinc}_{\pi_C}^{-1}$  denotes the inverse of the  $\text{sinc}_\pi$  function computed using the Cloude (2010) approach.  
 200 Similarly,  $\text{sinc}_{\pi_S}^{-1}$  represents the inverse of the  $\text{sinc}_\pi$  function obtained by applying the secant  
 201 method (Cheney & Kincaid, 2012; Jones et al., 2001). This root finding technique has been  
 202 deployed as it is more accurate than the given approximation in Eq. (2.4c), the analysis of  
 203 which is described in section 4.3.3. Still, in the Python implementation, this approximation  
 204 is used as an initial guess to the secant method for faster convergence. It is also used as a  
 205 fallback option if the secant method is unable to converge within 50 iterations or the default

206 convergence threshold of 1.4E-8 (Jones et al., 2001).

$$\text{sinc}_C^{-1}(\gamma(\vec{w}_v)) = \pi - 2 \sin^{-1}(\gamma(\vec{w}_v)^{0.8}) \quad (2.4a)$$

$$\text{sinc}_\pi \alpha_r - \gamma(\vec{w}_v) = 0 \quad (2.4b)$$

$$\text{sinc}_{\pi C}^{-1}(\gamma(\vec{w}_v)) = \frac{\text{sinc}_C^{-1}(\gamma(\vec{w}_v))}{\pi} \quad (2.4c)$$

### 207 2.3. Validation, Uncertainty Assessment, and Sensitivity Analysis

#### 208 2.3.1. Validation Process

209 One of the significant challenges in this work is the limited ground-truth data availability.  
 210 Since, in-situ data from only two ground stations are available, the conventional way of  
 211 accuracy assessment through regression plots (Kugler et al., 2015; Leinss et al., 2014; Kumar  
 212 et al., 2017) is infeasible in this context. Moreover, the Kothi AWS (Fig 3.1) area falls in the  
 213 layover region for the descending pass acquisitions and hence, only the Dhundi region which  
 214 is free from layover, shadow and foreshortening effects, is used for validation. In this case,  
 215 a neighbourhood window of size  $5 \times 5$  ( $\approx 225 \text{ m}^2$  ground area) surrounding the Dhundi SPA  
 216 is selected for validating the SSD and SSWE estimates by considering only the statistical  
 217 mean and standard deviation.

#### 218 2.3.2. Uncertainty Assessment

219 Due to the complex terrain characteristics there exist significant uncertainty sources  
 220 which could potentially lead to the overall degradation of the output accuracy. Having  
 221 the quad-pol data in winter time (January 8, 2016) and dual-pol data in summer time,  
 222 we are able to use dual-pol entropy ( $H \in [0, 1]$ ) and the scattering alpha angle ( $\alpha \in [0^\circ,$   
 223  $90^\circ]$ ) or  $H/\alpha$  decomposition to comparatively understand the backscattering mechanisms in  
 224 these two time intervals (Cloude, 2010; Lee & Pottier, 2009; Singh et al., 2014). The  $5 \times 5$   
 225 window size for the  $H/\alpha$  decomposition is used. This is carried out through the  $H/\alpha$  plane  
 226 plot which demarcates eight feasible zones (Z9 being the unclassified pixels) based on the  
 227 different scattering classes as shown in Figure 2.2. Note that, this diagram which follows  
 228 the SNAP style (ESA, 2019), uses slightly different labels as compared to the Lee & Pottier  
 229 (2009)  $H/\alpha$  plane convention where the labels Z1, Z2, Z3 are denoted as Z7, Z8, Z9 and  
 230 vice-versa respectively. However, the scattering mechanisms are exactly the same in both  
 231 these conventions. Also, the blue curve acts as a boundary to the plane which essentially  
 232 denotes the reliability of the classification in high entropy conditions (Brunner, 2009).

233 The dual-pol  $H/\alpha$  decomposition is further used by the unsupervised Wishart classifier  
 234 (ten iterations) which classifies the SAR data based on these scattering mechanisms and a  
 235 quantitative estimate of the number of pixels in each such class can be obtained (Cloude,  
 236 2010; Lee & Pottier, 2009). Therefore, by knowing the scattering properties, the terrain  
 237 features present in the study area can be understood along with their changes during the snow  
 238 season. In turn, these ground features which include rough surfaces, shrubs, boulders, and  
 239 human settlements reduce the Pol-InSAR surface coherence amplitude, ( $\gamma(\vec{w}_v) = |\tilde{\gamma}(\vec{w}_v)|$ )  
 240 which may result in overestimated volumetric height (SSD) (Cloude, 2010; Hajnsek et al.,  
 241 2009; Kugler et al., 2015). Hence, a summer and winter time surface coherence comparison



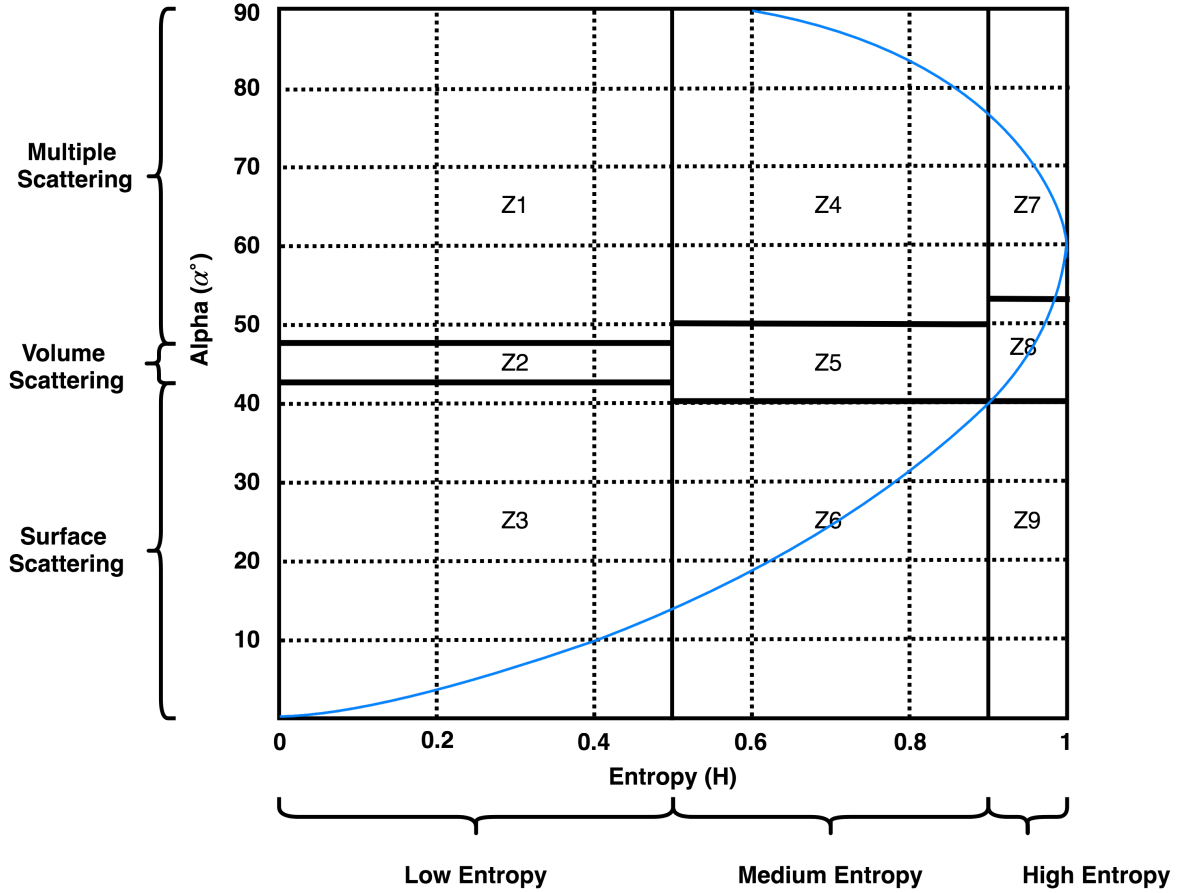


Figure 2.2:  $H/\alpha$  plane showing different scattering zones. Z1: Dihedral, Z2: Dipole, Z3: Bragg Surface, Z4: Double bounce, Z5: Anisotropic, Z6: Random surface, Z7: Complex structures, Z8: Random anisotropic, Z9: Non-feasible.

242 (volume coherence cannot be computed for the summer time datasets because these are dual-  
 243 pol, Table 3.1) is also performed to further analyse the effects of these ground features. Thus,  
 244 the uncertainty assessment by means of the identification of the backscattering mechanisms  
 245 constitutes a key role in this work.

246 Apart from this, the forest cover map (obtained from WRD, IIRS) along with the layover  
 247 and shadow regions computed using SAR simulation are used to mask out the noisy pixels  
 248 which degrade the quality of the results. This is a standard approach used in the studies  
 249 focusing on snow property estimation in forested or alpine terrains (Leinss et al., 2014, 2016;  
 250 Singh et al., 2017; Thakur et al., 2012; Usami et al., 2016).

### 251 2.3.3. Sensitivity Analysis

252 The variation of the SSD and SSWE values corresponding to the changes in the free  
 253 parameters in the SSD inversion model (window size, coherence threshold, scaling factors)  
 254 are observed by iteratively running the algorithm and computing the statistical mean and  
 255 standard deviation using the neighbourhood window discussed earlier in section 2.3.1. This  
 256 helps in deciding the window shape and sizes and also choosing the optimum values for the  
 257 several free parameters. Moreover, the accuracy of the root finding algorithm discussed in

section 2.2 is also checked for some possible coherence values (section 4.3.3).

In addition, the ground elevation measurements acquired during the field visit to Dhundi and Kothi were compared with the ALOS PALSAR DEM elevations ( $z$ ). The effect of the DEM errors on the LIA,  $\theta_l$ , is then checked for performing the sensitivity analysis using Eq. (2.5) which incorporates the slope angles in  $x$  ( $\omega_x$ ) and  $y$  ( $\omega_y$ ) directions (pixel co-ordinate system where  $z$  is the corresponding elevation value) derived from the DEM elevation values along with the radar incidence angle ( $\theta$ ) (Lee et al., 2000; Lee & Pottier, 2009). Here, the terms  $dz/dx$  and  $dz/dy$  refer to the rate of elevation ( $z$ ) change in the  $x$  and  $y$  directions respectively.

$$\theta_l = \cos^{-1} \frac{\cos \omega_x \cos (\omega_y - \theta)}{\sqrt{\cos^2 \omega_y \sin^2 \omega_x + \cos^2 \omega_x}} \quad (2.5)$$

where,

$$\omega_x = \tan^{-1} \frac{dz}{dx}, \omega_y = \tan^{-1} \frac{dz}{dy}.$$

### 3. Study Area, Datasets, and Software

#### 3.1. Chosen Study Area

##### 3.1.1. Geographical Situation

The Beas river watershed near Manali, India is part of the north-western Himalayas. Naturally, steep slopes and dense forests are prominent in this region. The elevation typically varies from nearly 2500 m to more than 5000 m in some places as observed in the reference ALOS PALSAR DEM (Figure 3.1).

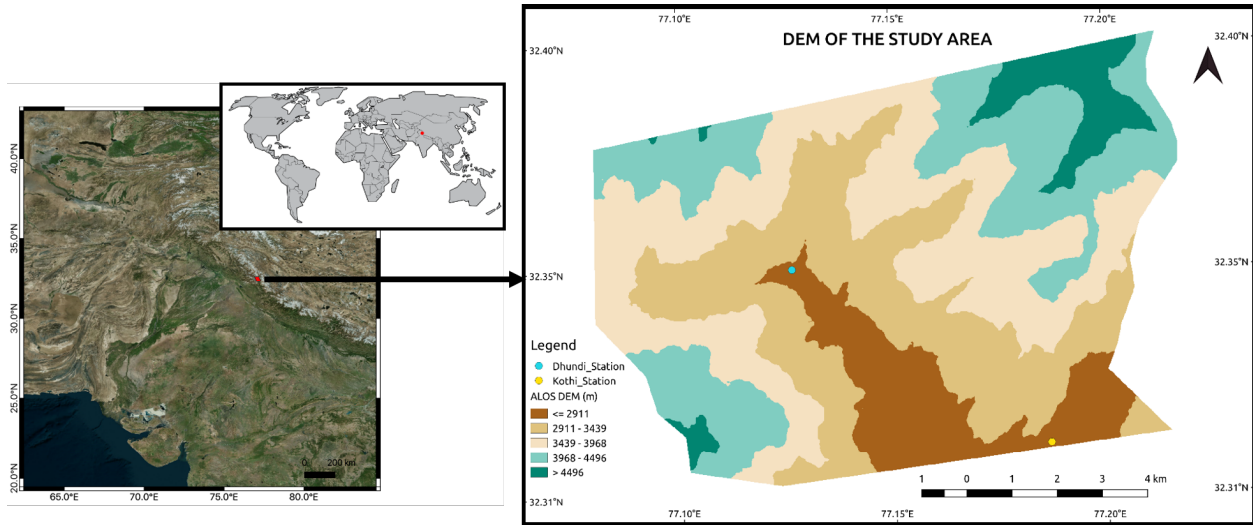


Figure 3.1: Overview map of the study area showing the ALOS PALSAR DEM. The original DEM of 12.5 m spatial resolution (generated in 2011) has been resampled to 3 m using bilinear interpolation (Wu et al., 2008) to match the high resolution SAR data. Moreover, the vertical resolution as per the product specification is 5 m.

In this work, a small region ( $\sim 96 \text{ km}^2$ ) of the Beas basin is chosen which starts a few kilometres uphill from Dhundi up to Kothi (shown in Figure 3.1). These areas receive

276 substantial seasonal snowfall which begins in December and lasts till late March. However,  
 277 the cold, dry season usually commences from late September or early October. The coldest  
 278 period is in January during which the temperatures reach a daily minimum of  $-15^{\circ}\text{C}$  on an  
 279 average. The summers are mild to occasionally warm with June being the hottest month  
 280 (mean and maximum temperatures of  $20^{\circ}\text{C}$  and  $30^{\circ}\text{C}$  respectively are common). Apart from  
 281 this, significant rainfall occurs between late June and September (monsoon season) with  
 282 August receiving the maximum precipitation (Majumdar et al., 2019a; Thakur et al., 2012).

### 283 3.1.2. Field Visit

284 Intensive fieldwork had been conducted from October 14-21, 2018 in the Dhundi and  
 285 Kothi areas where several Differential Global Positioning System (DGPS) measurements  
 286 were acquired using the Leica Viva GS 10 (Leica Geosystems AG, 2012) with adequate  
 287 horizontal positional accuracies ( $\sim 7$  cm) (Majumdar et al., 2019a). Due to the complex  
 288 terrains, most of the DGPS readings had been obtained through the kinematic mode (Luo  
 289 et al., 2014). However, in some of the convenient places such as the Dhundi base station  
 290 and near the Kothi Automatic Weather Station (AWS), the static mode was used (Leica  
 291 Geosystems AG, 2012). Eventually, elevation information from these DGPS points have  
 292 been compared with the ALOS PALSAR DEM, the details of which are provided in section  
 293 4.3.5. In order to properly understand and visualise the characteristics of the study area,  
 294 selected field photographs and their brief description are shown from figures 3.2(a)-3.2(f).

Table 3.1: Bistatic TerraSAR-X/TanDEM-X dataset metadata. The date and time are shown in DD/MM/YYYY and UTC hrs formats respectively.

Date	Time	Polarisation	Orbital Direction	$B_{\perp}$ (m)	$h_{2\pi}$ (m)
29/12/2015	12:46	Quad	Ascending	273.51	18.54
08/01/2016	00:53	Quad	Descending	96.34	63.18
09/01/2016	12:46	Quad	Ascending	288.29	17.61
19/01/2016	00:53	Quad	Descending	96.10	63.34
20/01/2016	12:46	Quad	Ascending	289.68	17.53
30/01/2016	00:53	Quad	Descending	98.15	62.02
06/01/2017	12:46	HH	Ascending	230.17	22.18
24/03/2017	12:46	Dual	Ascending	377.97	13.44
15/04/2017	12:46	Dual	Ascending	327.53	15.52
26/04/2017	12:46	Dual	Ascending	286.69	17.73
08/06/2017	00:53	Dual	Descending	93.09	65.37
24/08/2017	00:53	Dual	Descending	17.51	347.49

### 295 3.2. Datasets Used

296 Overall twelve Coregistered Single look Slant range Complex (CoSSC) TerraSAR-X  
 297 (TSX)/TanDEM-X (TDX) bistatic X-band SAR images acquired between December 2015  
 298 and August 2017 in stripmap (SM) mode are available over this study area (Balss et al.,  
 299 2012). The datasets are summarised in Table 3.1. In total, there are six Quad-pol data pairs  
 300 wherein the ascending and descending orbital pass acquisitions are at 12:46 hrs and 00:53



(a) DGPS positional accuracy checking



(b) Leica DGPS base



(c) Beas river



(d) Landscape and human settlements



(e) Mountains and forests



(f) Weather instruments

Figure 3.2: Dhundi field photographs showing the varying topographic features present in the surrounding area.

301 hrs Universal Time Coordinated (UTC) respectively. Moreover, the perpendicular baseline  
302 ( $B_{\perp}$ ) and ambiguity height ( $h_{2\pi}$ ) for these datasets are also provided in Table 3.1.

303 Additionally, the high frequency data (two-minute interval measurements) obtained from  
304 the snowpack analyser (SPA) device (installed at Dhundi) had been downloaded and were  
305 added to the database as a separate table. Accordingly, the in-situ SSDs and snow densities  
306 at 06:22 hrs (00:52 hrs UTC) and 18:16 hrs (12:46 hrs UTC) Indian Standard Time (IST)  
307 for the descending and ascending pass acquisitions respectively have been considered. The  
308 in-situ SSDs along with the corresponding snow densities and SSWEs are provided in Table  
309 3.2. Apart from this, a forest mask used in previous studies involving this watershed area  
310 (Thakur et al., 2012, 2017) has been obtained from the Water Resources Department (WRD),

311 Indian Institute of Remote Sensing (IIRS).

Table 3.2: In-situ SSD, snow density, and SSWE measured by the SPA instrument at the Dhundi site. The date and time are in DD/MM/YYYY and UTC hrs respectively.

Date	Time	SSD (cm)	Snow Density (g/cm <sup>3</sup> )	SSWE (mm)
29/12/2015	12:46	36.70	0.382	140.19
08/01/2016	00:52	54.90	0.315	172.94
09/01/2016	12:46	56.00	0.304	170.24
19/01/2016	00:52	42.80	0.347	148.52
20/01/2016	12:46	42.80	0.338	144.66
30/01/2016	00:52	70.00	0.210	147.00

312 The Sentinel Application Platform (SNAP) 7.0.0 (ESA, 2019) has been used for basic  
 313 SAR processing. In addition, the SSD inversion model has been implemented using Python  
 314 3 wherein PyCharm Community Edition 2019.3.1 (JetBrains, 2020) was used as the coding  
 315 environment. Moreover, the final snow depth maps have been prepared using QGIS 3.10  
 316 (QGIS Development Team, 2019). Furthermore, some of the computationally intensive tasks  
 317 have been carried out using the High-Performance Computing (HPC) infrastructure installed  
 318 at IIRS.

## 319 4. Results and Discussion

### 320 4.1. Scattering Mechanisms

321 The winter (January 8, 2016) and summer-time (June 8, 2017) dual-pol  $H/\alpha$   
 322 decomposition (Figure 4.3) and unsupervised Wishart classification (Figure 4.1) results  
 323 combined with the derived class percentage statistics (Figure 4.2) show that, in the presence  
 324 of snow, the high entropy anisotropic volume scattering (Z8) increases by 5.11% whereas  
 325 the medium entropy volume scattering (Z5) decreases by 7.01% for the entire study area.  
 326 This reduction in the Z5 volume scattering could be attributed to the partially snow covered  
 327 forests and shrubs which exhibit higher volume scattering at X-band during the snow-free  
 328 season (Figure 3.2(e)). The corresponding dual-pol Wishart classified maps are displayed  
 329 along with the zoomed views in Figure 4.1(a) and Figure 4.1(b) respectively.

330 Moreover, the Bragg surface scattering (Z3) is slightly higher in summer (10.88%) as  
 331 compared to the winter (10.38%). One plausible reason for this is the 20 mm rainfall which  
 332 occurred on June 7, 2017, evening (data retrieved from the Dhundi record book). Also,  
 333 the occurrence of fresh snowfall in areas which did not have prior standing or old snow  
 334 would result in surface scattering from the ground (instead of volume scattering if standing  
 335 snow was present)(Leinss et al., 2014). Apart from this, the asbestos gable roofs used in  
 336 the human settlements (Figure 3.2(b) and Figure 3.2(d)) are strong single-bounce surface  
 337 scatterers (Brunner, 2009).

338 However, with snow accumulation on these materials, the surface scattering could be  
 339 reduced. Another prominent feature noticeable in Figure 4.1(b) is the high amount of surface  
 340 scattering from the river bed (Figure 3.2(c)) during the summer season. This is caused by  
 341 both the boulders and the increasing flow of snow-melt water in the river (Figure 3.2(c)).

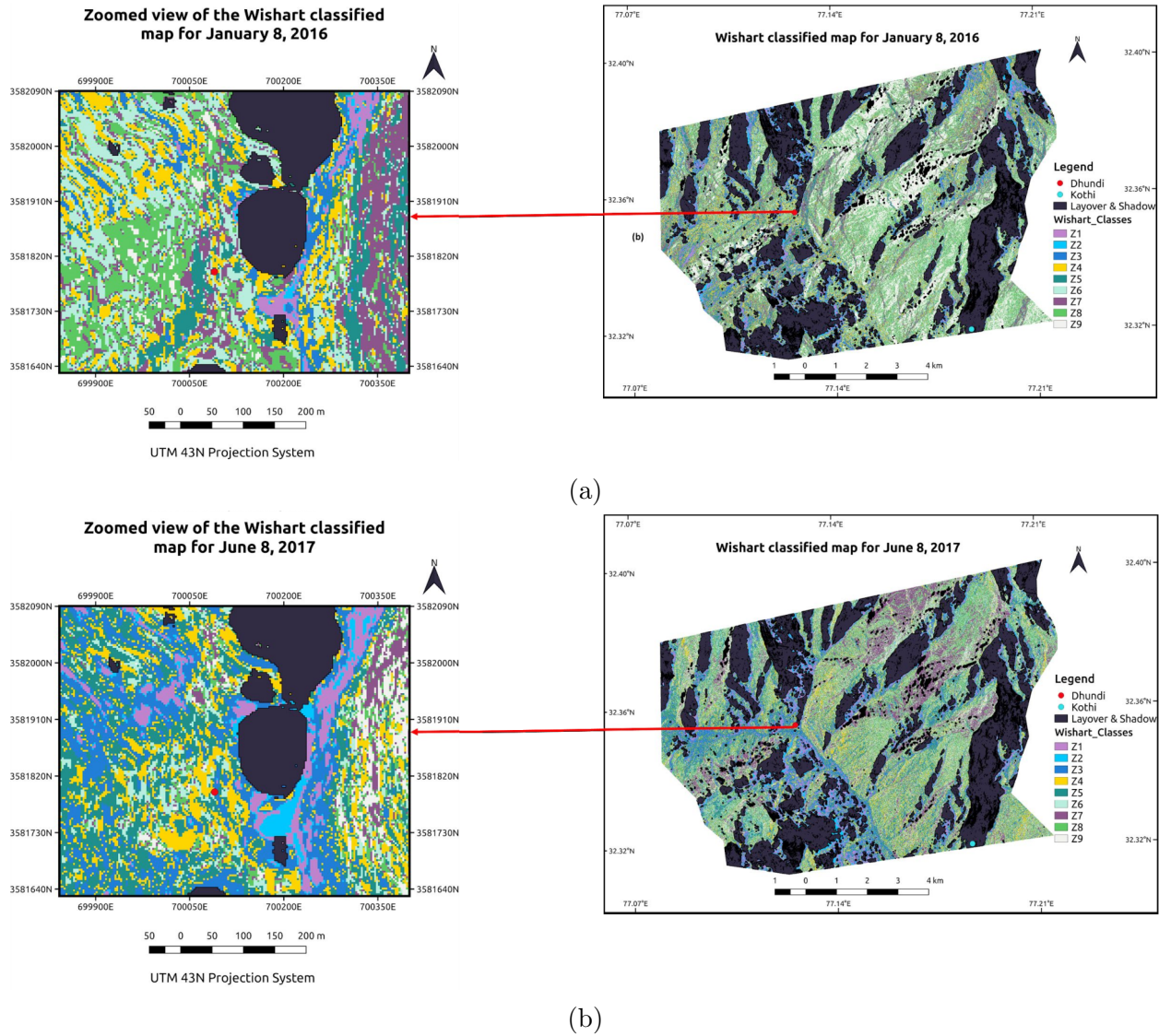


Figure 4.1: Zoomed views over Dhundi of the Wishart classified maps for the (a) January 8, 2016, and (b) June 8, 2017 data. In these maps, only the layover and shadow mask has been applied. Also, the Kothi area is excluded from the analysis since it lies in the layover region.

342 Furthermore, the human settlements result in double-bounce scattering (Z4) (Brunner,  
 343 2009), which in the winter-time scenario reduces by 0.34%. Also, the random surface  
 344 scattering (Z6) increases by 0.66% which could be caused by the presence of small snow  
 345 patches on the ground. Other than this, there is a strong decrease in the low entropy  
 346 multiple (dihedral) scattering from 8.23% to 5.17% in the snow-covered season which could  
 347 be caused by the added snow layer on the buildings and also boulders.

348 Another interesting aspect in this context is the increase (from 9.93% to 19.8%) in the  
 349 number of unclassified or non-feasible pixels (Z9) for the winter-time image (Figure 4.2)  
 350 which is also depicted through the  $H/\alpha$  plane plots in Figure 4.3(a) and Figure 4.3(b). This  
 351 is primarily resulting from the added terrain complexity owing to the snow accumulation.  
 352 In order to resolve this issue, the quad-pol entropy ( $H$ ), anisotropy ( $A \in [0, 1]$ ), alpha ( $\alpha$ ),

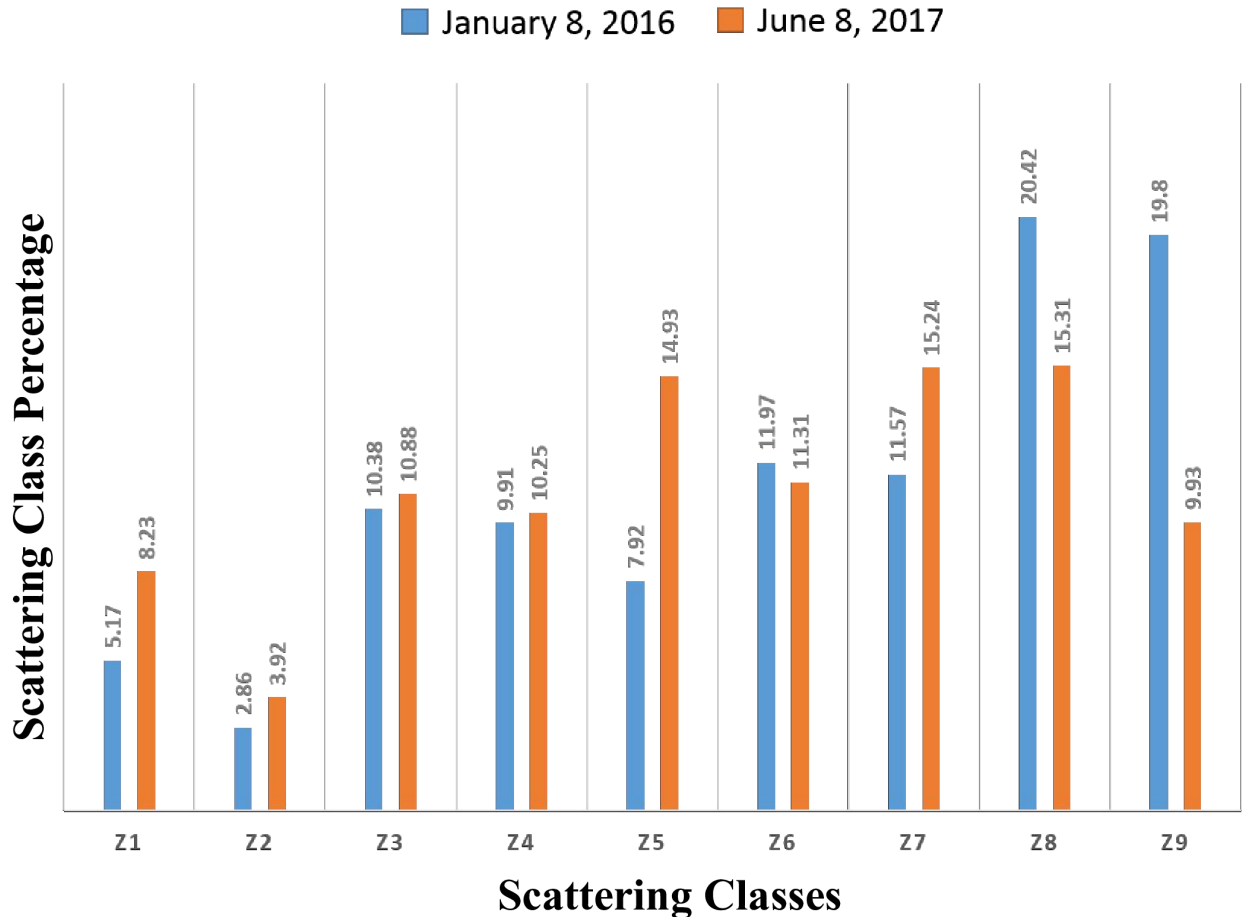


Figure 4.2: Scattering class percentages (rounded to 2 decimal places) from the unsupervised Wishart classification. The different zone labels are described in Figure 2.2.

353  $H/A/\alpha$  decomposition has been applied on the January 8, 2016 data. The corresponding  
 354  $H/\alpha$  plane plot in Figure 4.3(c) shows that the quad-pol approach is able to fully classify  
 355 the winter-time image. However, since the summer-time image is having only HH and VV  
 356 channels, the dual-pol method has been used to properly compare the respective scattering  
 357 mechanisms (Majumdar et al., 2019a).

358 Thus, from this discussion, it is clearly observed that the presence of snow causes  
 359 a substantial change of the scattering patterns in the study area resulting in significant  
 360 uncertainty sources. In turn, the optimisation of the model parameters along with the  
 361 sensitivity analysis of the SSD values depend on these scattering types. As an example, if  
 362 there is low volume scattering, the SSD results are generally underestimated (Cloude, 2005;  
 363 Hajnsek et al., 2009; Kugler et al., 2015). Therefore, the uncertainty assessment by means  
 364 of the scattering mechanism classification is one of the key aspects of this research.

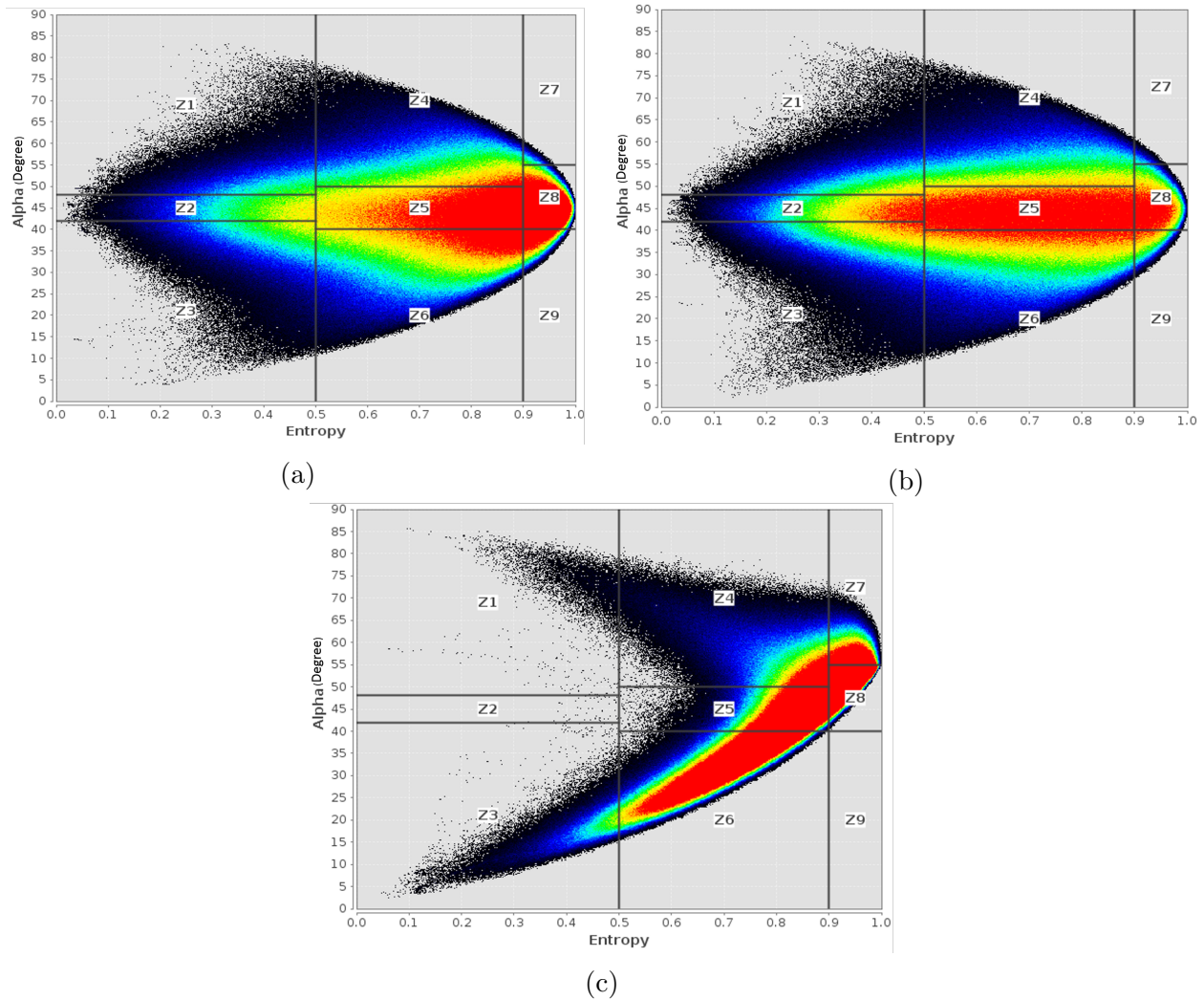


Figure 4.3: Dual-pol  $H/\alpha$  plane plots for the (a) January 8, 2016, and (b) June 8, 2017 data, (c) Quad-pol  $H/\alpha$  plane plot for the January 8, 2016 data. The colours red, green, blue, and black indicate the point density with red being the highest, and black as the lowest. These plots have been made using SNAP (ESA, 2019).

#### 365 4.2. Changes in Surface Coherence

366 The summer (June 8, 2017) and winter (January 8, 2016) surface coherences are compared  
 367 in Fig 4.4 which indicate higher surface coherence values for the summer time image (Fig  
 368 4.4(b)). These surface coherences are computed only from the VV channel using standard  
 369 InSAR workflow in SNAP (ESA, 2019). The visual analysis suggests that the surface  
 370 coherence is higher (implying higher surface scattering) during June 8, 2017 which is in  
 371 concordance with the backscattering mechanisms discussed in the previous section (Fig 4.1).  
 372 Accordingly, the mean surface coherence (calculated using the same  $5 \times 5$  window) is reduced  
 373 from  $\sim 0.62$  to  $\sim 0.60$  during the winter time (Fig 4.4(a)) due to the presence of standing  
 374 snow. However, this reduction is small owing to the surface scatterers (e.g., gable roofs, Fig  
 375 3.2(b)) such as the ones present near the Dhundi base station.



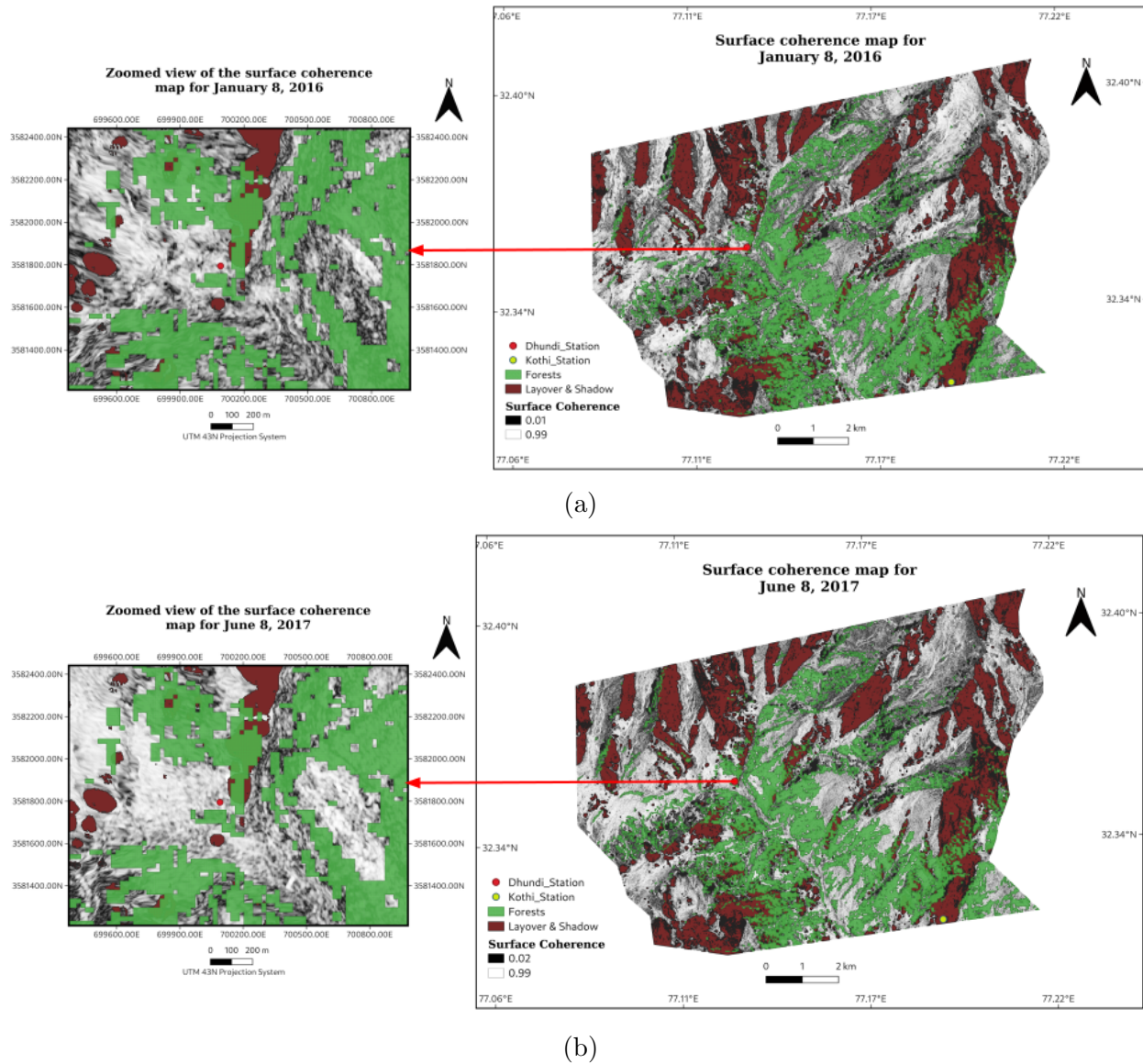


Figure 4.4: Zoomed views over Dhundi of the surface coherence maps for the (a) January 8, 2016, and (b) June 8, 2017 data.

### 376 4.3. Sensitivity Analysis Results

377 In order to perform the sensitivity analysis, only the Dhundi area is chosen for validation.  
 378 Accordingly, the MAE calculated from all the SSD estimates is used for optimising the model  
 379 parameters.

380 The SSD inversion model as described from the implementation or methodological  
 381 perspective in section 2.2 incorporates several user-defined free parameters. Thus, it is  
 382 necessary to conduct an appropriate sensitivity analysis for the hybrid Pol-InSAR based  
 383 volumetric height (SSD) retrieval algorithm. Accordingly, the various model parameters and  
 384 their optimisation are discussed below.

#### 4.3.1. Volume and Surface Coherence Ensemble Window

The ensemble windows corresponding to the number of looks ( $L$ ) in Eq. (2.1a) must be suitably chosen so as to maximise both the volume coherence amplitude,  $\gamma(\overline{w}_v)$ , and the surface coherence amplitude,  $\gamma(\overline{w}_s)$ . As a result, the sensitivity analysis for these window sizes is an important aspect of this work.

The effects of  $L$  on the mean volume coherence amplitude,  $\mu_{\gamma(\overline{w}_v)}$  and the mean surface coherence amplitude,  $\mu_{\gamma(\overline{w}_s)}$  which are measured by applying the same  $5 \times 5$  neighbourhood window over Dhundi (section 2.2) along with the respective standard deviations,  $\sigma_{\gamma(\overline{w}_v)}$  and  $\sigma_{\gamma(\overline{w}_s)}$ , are displayed in Figure 4.5.

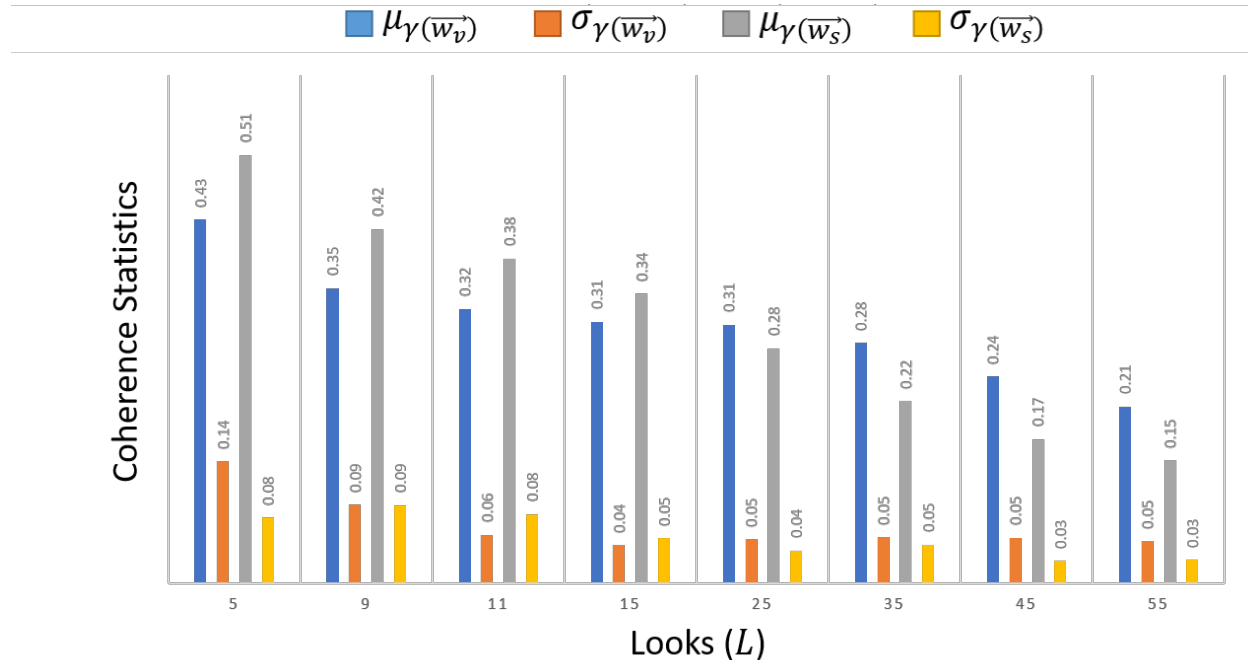


Figure 4.5: Effect of the number of looks ( $L$ ) on the volume and surface coherence for January 8, 2016. All the values are rounded to 2 decimal places. Similar statistics were obtained for other datasets.

It can be seen that for the executed test cases, with increasing  $L$ , there is a general decreasing trend for both these coherences. So, for the SSD estimation,  $L = 5$  is chosen which is unbiased since  $L > 3$  (Cloude, 2010). This is because,  $\sigma_{\gamma(\overline{w}_v)} \approx 0.14$  and  $\sigma_{\gamma(\overline{w}_s)} \approx 0.08$  are sufficiently small with adequately high  $\mu_{\gamma(\overline{w}_v)} \approx 0.43$  and  $\mu_{\gamma(\overline{w}_s)} \approx 0.51$ .

However, there exist several free parameters in this Pol-InSAR based SSD inversion model (section 2.2) and hence, the volume and surface coherence ensemble windows need to be kept constant ( $L = 5$ ) for the subsequent sensitivity analyses of the other parameters.

#### 4.3.2. Scaling Parameters

It has been previously discussed in section 2.2 that there are two scaling parameters involved in the SSD estimation process. These are the vertical wavenumber scaling parameter ( $\eta' \in \mathbb{R}_{>0}^+$ ) and the scaling factor ( $\eta \in [0, 1]$ ) of the hybrid DEM differencing approach developed by Cloude (2010). More specifically, the optimised  $\eta'$  values for each acquisition

406 are described in Table 4.1. We see that these optimised values do not significantly vary for  
 407 each acquisition type, i.e.,  $\eta' \in \{6, 8, 9\}$  and  $\eta' \in \{16, 19\}$  for ascending and descending  
 408 pass acquisitions respectively (Table 3.1). However, for the December 29, 2015 acquisition,  
 409  $k_z$  was prescaled by 10 because the actual  $k_z < 0.01$  rad/m for this dataset was very low as  
 410 compared to the other datasets wherein  $k_z \in (0.1, 0.3)$  rad/m. Also,  $L = 5$ , ground phase  
 411 median ensemble filter window ( $5 \times 5$ ), vertical wavenumber ensemble average window ( $5 \times 5$ ),  
 412 and the SSD ensemble average window of size  $5 \times 5$  are unchanged during this sensitivity  
 413 analysis. So, only  $\eta'$  is optimised considering the MAE of all the SSD estimates.

Table 4.1: Optimised vertical wavenumber scaling factors for each acquisition.

Date	Orbital Direction	$\eta'$
29/12/2015	Ascending	9
08/01/2016	Descending	19
09/01/2016	Ascending	6
19/01/2016	Descending	16
20/01/2016	Ascending	8
30/01/2016	Descending	19

414 Next, the monotonically increasing SSD with respect to increasing  $\eta$  are displayed in  
 415 Figure 4.6 for the January 8, 2016 acquisition. Similar results are obtained for the other  
 416 datasets also and hence, those are not discussed here. For  $\eta = 0$ , the standard DEM  
 417 differencing technique (Cloude, 2005) results in the mean SSD,  $\mu_s \approx 43.08$  cm with the  
 418 corresponding SSD standard deviation,  $\sigma_s \approx 7.40$  cm. As the SPA measured SSD at 00:52  
 419 hrs UTC, January 8, 2016, is 54.90 cm (Table 3.2), so  $\mu_s$  is underestimated. Naturally, the  
 420 mean SSWE,  $\mu_{ss} \approx 135.69$  mm (with SSWE standard deviation,  $\sigma_{ss} \approx 23.30$  mm) is also  
 421 lower compared to the SPA measured SSWE of 173 mm. Thus, to effectively optimise the  
 422 SSD,  $\eta$  needs to be suitably increased (Cloude, 2005, 2010).

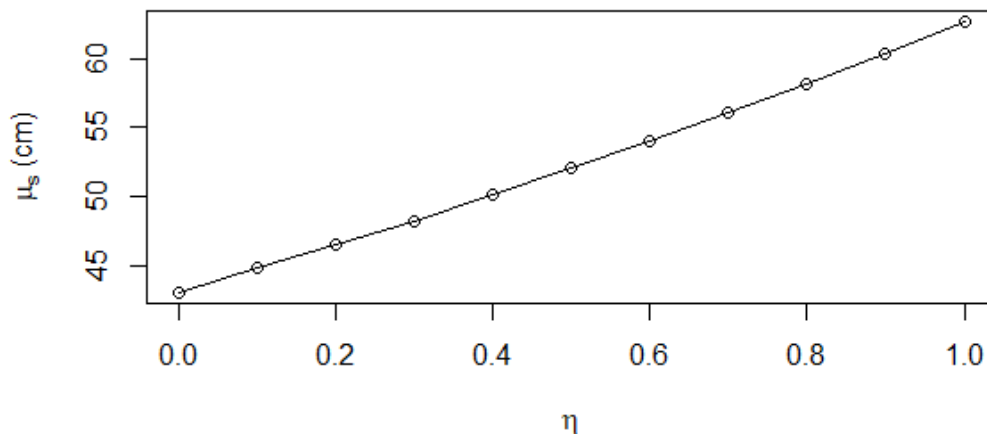


Figure 4.6: Increasing mean SSD ( $\mu_s$ ) for January 8, 2016 with respect to the scaling parameter  $\eta$ .  $\eta = 0.6$  is chosen as the optimal value for all the datasets.

423 In this context, Cloude (2005) has suggested setting  $\eta = 0.4$  for which the accuracy  
 424 of the estimated tree height is found to be more than 90%. Although by keeping  $\eta =$

425 0.4,  $\mu_s \approx 50.09$  cm ( $\sigma_s \approx 9.31$  cm) is obtained with  $\sim 91.23\%$  accuracy, the complexity of  
 426 the snow microstructure, anisotropy, and length scales necessitates the need for achieving  
 427 even higher accuracies (Leinss et al., 2016). Moreover, in the presence of significantly  
 428 varying hydrometeorological conditions which include high surface roughness and associated  
 429 uncertainty sources (section 4.1), the volume and surface coherence amplitudes generally do  
 430 not reach expected values of higher than 0.8 (Cloude, 2005; Kugler et al., 2015). Therefore,  
 431 with  $\eta = 0.6$ , the best SSD and SSWE accuracies of 98.43% ( $\mu_s \approx 54.04$  cm) and 98.39%  
 432 ( $\mu_{ss} \approx 170.22$  mm) respectively are achieved over Dhundi (for January 8, 2016) with  
 433 moderately low standard deviations ( $\sigma_s \approx 10.61$  cm,  $\sigma_{ss} \approx 33.41$  mm) accounting for good  
 434 reliability. Therefore, these results highlight the significance of this scaling parameter  $\eta$   
 435 towards controlling the snow structural height variations (Cloude, 2005, 2010) and hence,  
 436 the robustness of the hybrid DEM differencing model (section 2.2) is verified.

### 437 4.3.3. Computing sinc Inverse

438 In order to test the accuracy of the  $\text{sinc}_\pi$  inverse function, sample test data representing  
 439 the actual inverse,  $\alpha_r$ , have been prepared as shown in Table 4.2. Next, the  $\text{sinc}_\pi$  of these  
 440 data,  $\text{sinc}_\pi(\alpha_r)$ , is computed which essentially corresponds to the possible  $\gamma(\vec{w}_v)$  values. So,  
 441 the idea of performing sensitivity analysis in this scenario is to check the accuracy of the  
 442 calculated  $\text{sinc}_{\pi_C}^{-1}$  (Eq. (2.4c)) and  $\text{sinc}_{\pi_S}^{-1}$  (Eq. (2.4b)) of the  $\text{sinc}_\pi(\alpha_r)$  values by comparing  
 443 these with  $\alpha_r$ .

Table 4.2: Comparison between the normalised Cloude (2010) sinc inverse and the secant sinc inverse methods.

$\alpha_r$ (rad)	$\text{sinc}_\pi(\alpha_r)$	$\text{sinc}_{\pi_C}^{-1}$ (rad)	$\text{sinc}_{\pi_S}^{-1}$ (rad)
0.1	0.984	0.103	0.100
0.2	0.935	0.206	0.200
0.3	0.858	0.308	0.300
0.4	0.757	0.409	0.400
0.5	0.637	0.509	0.500
0.6	0.505	0.607	0.600
0.7	0.368	0.703	0.700
0.8	0.234	0.798	0.800
0.9	0.109	0.891	0.900

444 From Table 4.2 it is observed that the secant method converges exactly (up to 13 decimal  
 445 places) to the actual  $\alpha_r$  while the normalised Cloude (2010) approximation of the  $\text{sinc}_\pi$  inverse  
 446 has some minute errors involved (RMSE  $\approx 0.02$  rad). Similarly, the sinc function is tested  
 447 (Table 4.3) where  $\text{sinc}_C^{-1}$  and  $\text{sinc}_S^{-1}$  denote the standard Cloude (2010) approximation (Eq.  
 448 (2.4a)) and the secant method of root finding for the traditional sinc function respectively.  
 449 Again, the secant method exactly converges (up to 13 decimal places) whereas RMSE  $\approx 0.02$   
 450 rad is associated with the  $\text{sinc}_C^{-1}$ . The computed results shown in Table 4.2 and Table 4.3  
 451 are rounded to 3 decimal places.

452 Therefore, by performing the sensitivity analysis of the  $\text{sinc}_{\pi_C}^{-1}$ ,  $\text{sinc}_{\pi_S}^{-1}$ ,  $\text{sinc}_C^{-1}$ , and  $\text{sinc}_S^{-1}$ ,  
 453 it is clearly understood that the secant method provides highly accurate results. Hence, in

Table 4.3: Comparison between the traditional Cloude (2010) sinc inverse and the secant sinc inverse methods.

$\alpha_r$ (rad)	$\text{sinc}(\alpha_r)$	$\text{sinc}_C^{-1}$ (rad)	$\text{sinc}_S^{-1}$ (rad)
0.1	0.998	0.103	0.100
0.2	0.993	0.207	0.200
0.3	0.985	0.310	0.300
0.4	0.974	0.413	0.400
0.5	0.959	0.516	0.500
0.6	0.941	0.618	0.600
0.7	0.920	0.721	0.700
0.8	0.897	0.823	0.800
0.9	0.870	0.925	0.900

454 this work,  $\text{sinc}_{\pi_S}^{-1}$  is applied for solving Eq. (2.2a) wherein the  $\text{sinc}_{\pi_C}^{-1}(\gamma(\vec{w}_v))$  value is used  
 455 as an initial guess to the secant method for faster convergence.

#### 456 4.3.4. SSD Ensemble Window

457 Another essential free parameter used in the Pol-InSAR based SSD estimation model  
 458 (section 2.2) is the SSD ensemble averaging window size. By keeping  $\eta = 0.6$ ,  $\eta'$  values as in  
 459 Table 4.1, and other ensemble window sizes constant ( $5 \times 5$ ), the sensitivity analysis has been  
 460 carried out to observe the SSD variations which are shown in Figure 4.7 for the January 8,  
 461 2016 dataset.

462 The graphical representation in Figure 4.7 shows that when the window size is increased  
 463 beyond  $9 \times 9$ , the SSD values decrease sharply whereas, between the windows  $5 \times 5$  and  $9 \times 9$ ,  
 464 the values are consistent with the actual SSD measurement of 54.9 cm. This could be  
 465 attributed to the fact that, in mountainous terrains, elevation, and not distance, plays a  
 466 critical role in controlling the snow accumulation (Liu et al., 2017; Singh et al., 2014, 2017;  
 467 Thakur et al., 2012). The varying topographical conditions prominently visible in Figure  
 468 3.2 also ascertain that for larger window sizes, the snow depth variability could increase if  
 469 a nearby mountain also lies within the neighbourhood window or fluctuate due to changes  
 470 in volume coherence. So, considering these aspects, the ensemble window size of  $5 \times 5$  is  
 471 selected which results in  $\mu_s \approx 54.04$  cm with  $\sigma_s \approx 10.61$  cm as discussed in the scaling  
 472 parameter sensitivity analysis. It is noteworthy that similar observations were made for the  
 473 other datasets.

#### 474 4.3.5. DEM and LIA Error Analysis

475 During the field visit (section 3.1.2), several DGPS points which had been acquired are  
 476 used to check the accuracy of the ALOS PALSAR DEM (Fig 3.1). In essence, the observed  
 477 errors are then used to analyse the change in the LIA (Eq. (2.5)) induced by the corrected  
 478 DEM (the erroneous DEM pixels are replaced by the respective DGPS measurements).

479 The DEM errors calculated using the Dhundi and Kothi DGPS readings are displayed in  
 480 Figure 4.8(a) and the subsequent LIA differences (computed from the corrected and original  
 481 DEMs) for these points are shown in Figure 4.8(b). As seen from these graphs, the absolute  
 482 elevation errors range from 0.08 m to 16.30 m in the Dhundi region, whereas these vary from

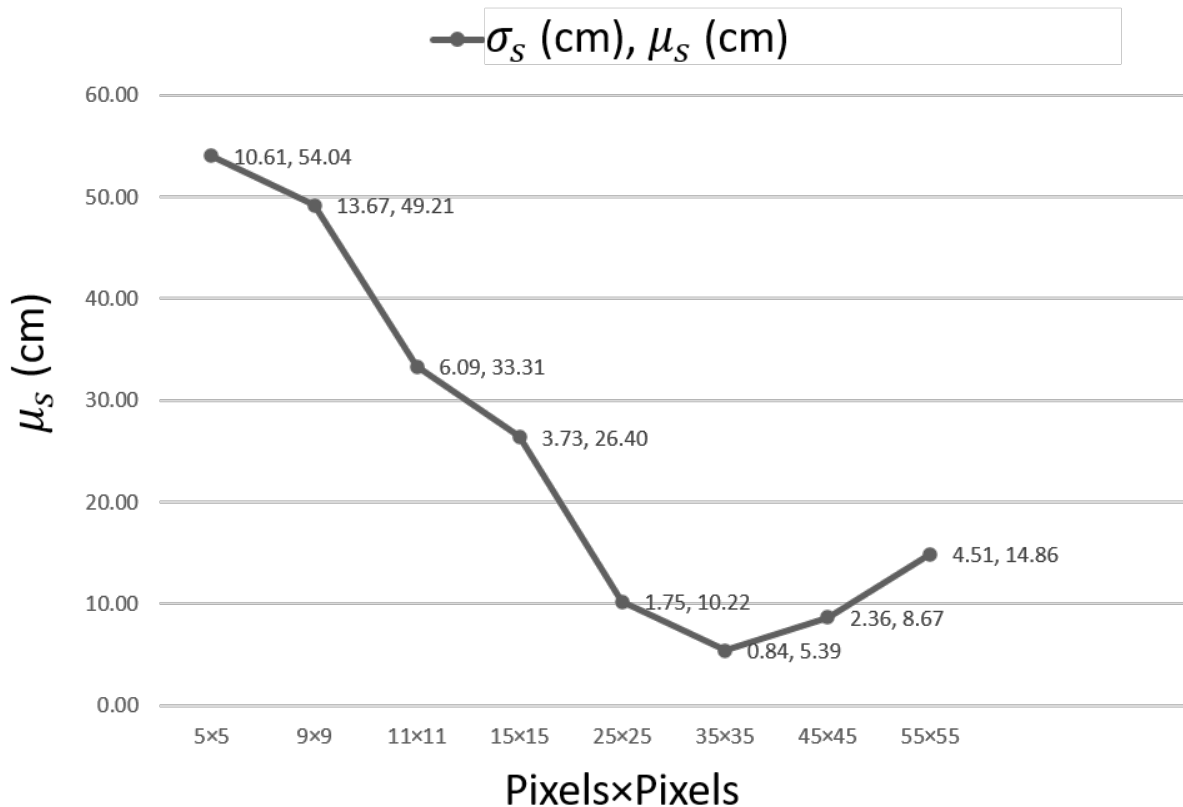
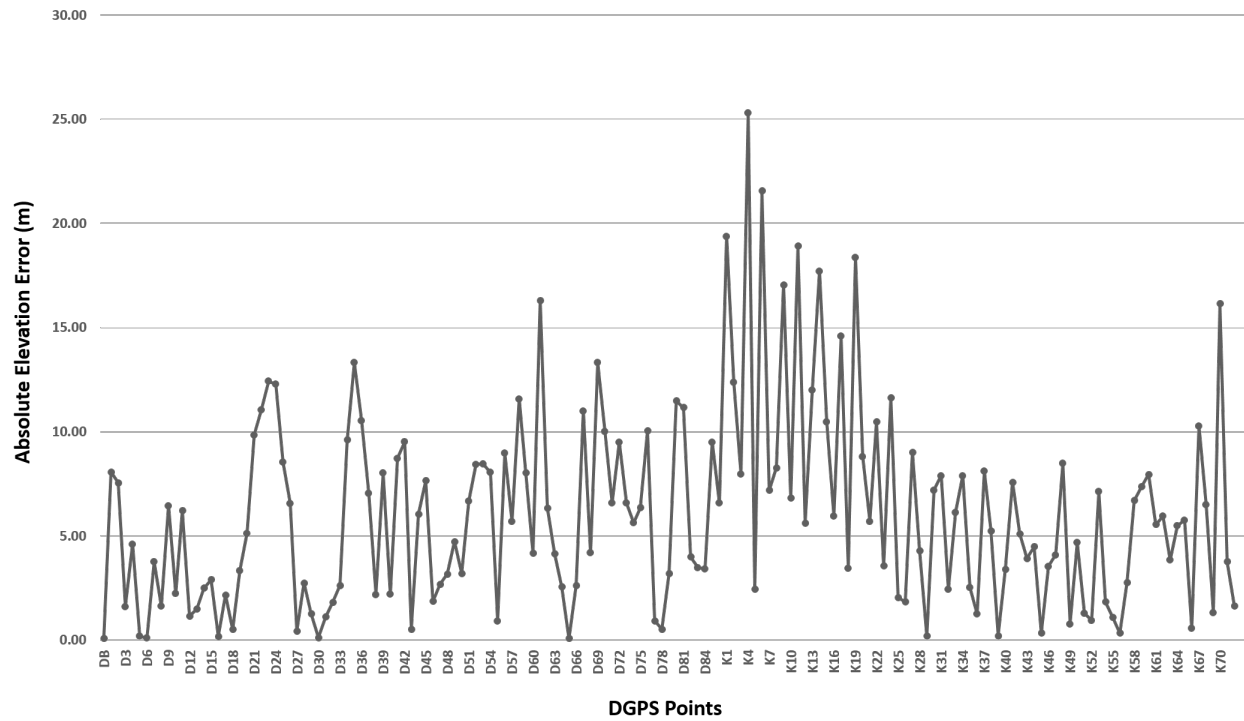


Figure 4.7: Effect of the ensemble window size on the SSD values for January 8, 2016.

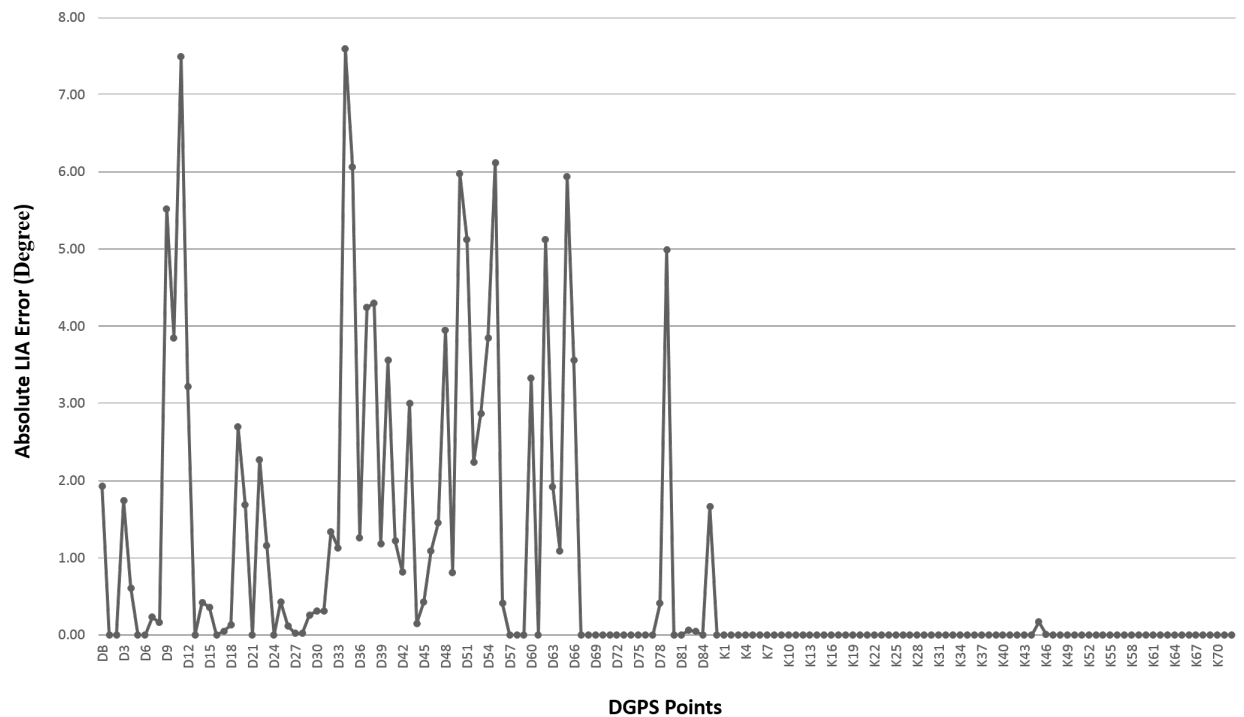
483 0.19 m to 25.32 m in the Kothi area. Accordingly, the RMSE values for the elevation errors  
 484 are approximately 6.71 m and 8.8 m respectively.

485 In addition, the LIA errors vary from  $0^\circ$  to  $7.59^\circ$  (Dhundi) and  $0^\circ$  to  $0.17^\circ$  (Kothi) in  
 486 these areas with the corresponding RMSE being nearly  $2.54^\circ$  and  $0.02^\circ$ . Since only the pixels  
 487 corresponding to the ground surveyed points are replaced with the modified LIA, so while  
 488 calculating the slope, the errors may not be large because the neighbouring pixels could  
 489 still have associated LIA errors which remain uncorrected. Thus, when the LIA errors are  
 490 rounded to 2 decimal places as in Fig 4.8(b), several values are exactly  $0^\circ$ . Furthermore, as  
 491 the LIA is dependent on the slope values (Eq. (2.5)), the DEM errors do not significantly  
 492 influence the LIA. Also, in the vertical wavenumber calculation used in the SSD estimation  
 493 given by Eq. (2.2b), the sine (sin) of the LIA is considered. So, the minute changes in the  
 494 LIA do not strongly affect the SSD estimates which are obtained after applying sufficient  
 495 ensemble averaging operation (section 2). Evidently, the LIA only changes by about  $1.9^\circ$   
 496 near the Dhundi base station and hence, the SSD results are not exhibiting any sizeable  
 497 impact from the associated DEM errors.

498 Therefore, the sensitivity analysis concerning the DEM errors and its propagation  
 499 highlights that the subsequent LIA errors are not directly governed by the changes in the  
 500 elevation values, rather the slopes in  $x$  and  $y$  directions (section 2.3.3) act as the primary  
 501 error sources. Also, the ALOS PALSAR DEM is sufficiently accurate even in the complex  
 502 terrains and hence, its usage in the LIA computation is justified.



(a)



(b)

Figure 4.8: (a) Absolute DEM errors obtained by comparing ALOS PALSAR DEM and the DGPS measurements and (b) observed absolute LIA errors. Here, DB is the Dhundi base station point, D1-D86 are acquired in the Dhundi region, and K1-K72 are measured in the Kothi area using the DGPS. All these values are rounded to 2 decimal places.

#### 4.4. Comparative Analysis of the Estimates

In order to visually observe the spatial patterns, the SSD maps for all the datasets were prepared but only the January 8, 2016 map is shown in Figure 4.9. The respective SSWE maps are not provided as these have been computed by multiplying the constant standing snow densities (Table 3.2) to the SSD values. Therefore, they have similar spatial characteristics like those of the snow depth maps.

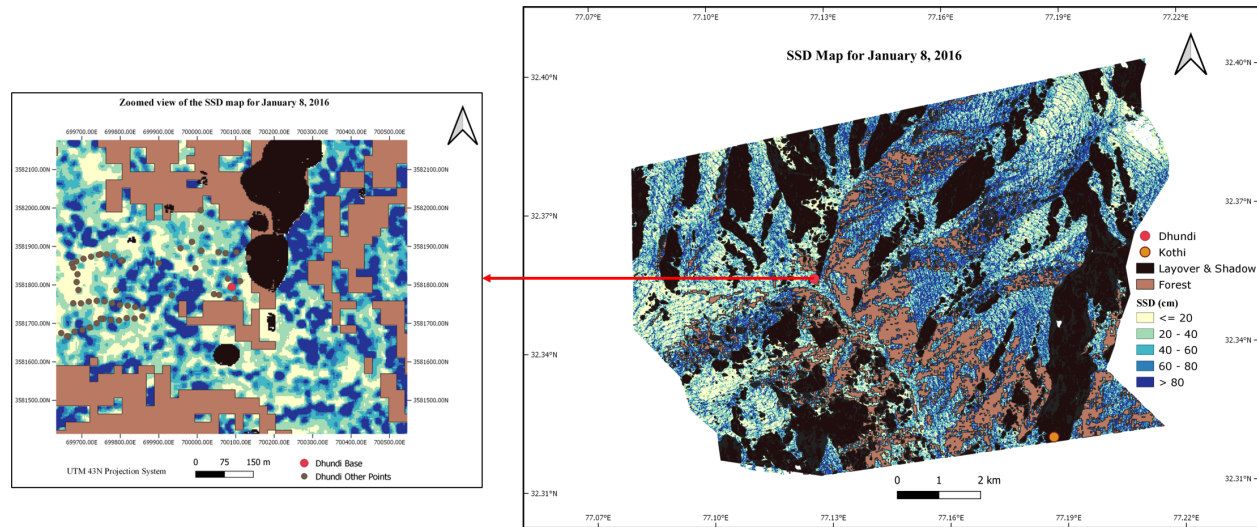


Figure 4.9: Zoomed view of the SSD map for January 8, 2016. The ground points surveyed (section 3.1.2) are shown wherein the closely spaced points have been acquired using the DGPS kinematic mode and fall on the nearby roads in the Dhundi region. The other points including the Dhundi base are measured using the static mode. Since the Kothi area falls in the layover and shadow zone, it is excluded from the zoomed view analysis. The significant SSD variations can be well observed from the zoomed map which showcase the challenges involved in appropriately modelling snow depth using Pol-InSAR over complex terrains.

The complete analysis of all the datasets are provided in Table 4.4 which shows that for the Dhundi site, the improved model displays sufficiently high overall SSD accuracy with coefficient of determination ( $R^2 \approx 0.96$ , MAE  $\approx 1.61$  cm, and Root Mean Square Error (RMSE)  $\approx 2.16$  cm. The corresponding SSWE estimates have  $R^2 \approx 0.71$ , MAE  $\approx 5.19$  mm, and RMSE  $\approx 6.84$  mm. This reduction in the  $R^2$  for the SSWEs indicate that even small errors present in the SSD estimates can greatly influence the estimated SSWEs. In Table 4.4,  $\epsilon_s$  and  $\epsilon_{ss}$  are the SSD and SSWE errors respectively with  $\mu_s$ ,  $\mu_{ss}$ ,  $\sigma_s$ , and  $\sigma_{ss}$  having same meanings as in section 4.3.2.

Moreover, the large variations in the SSD and SSWE for the complete region (Fig 4.9) highlight the extreme topographical conditions present in the study area. These variations can be confirmed from the ground survey (section 3.1.2) where the points (shown in Figure 4.9) had been acquired by considering the terrain undulations. Also, the aspect, slope, and elevation significantly influence the SSD estimates, the details of which have been discussed in the previous section.

Apart from this, it was observed that these estimates are lower in the Dhundi base station area as compared to the surrounding regions. This phenomenon can be attributed to the presence of the human settlements (Figure 3.2(b)) near the base point and are expected to have less snow accumulation than the natural surroundings. Moreover, the effect of multiple



Table 4.4: Accuracy assessment of the SSD and SSWE estimates in the Dhundi region. Here, the negative and positive errors represent overestimation and underestimation respectively. The date is represented in DD/MM/YYYY format and all the values are rounded to 2 decimal places.

Date	$\mu_s$ (cm)	$\sigma_s$ (cm)	$\epsilon_s$ (cm)	$\mu_{ss}$ (mm)	$\sigma_{ss}$ (mm)	$\epsilon_{ss}$ (mm)
29/12/2015	36.36	12.19	0.34	138.91	46.58	1.29
08/01/2016	54.04	10.61	0.86	170.22	33.41	2.71
09/01/2016	51.81	14.76	4.19	157.49	44.88	12.75
19/01/2016	41.46	12.96	1.34	143.88	44.97	4.64
20/01/2016	40.04	11.69	2.76	135.33	39.52	9.34
30/01/2016	70.19	24.01	-0.19	147.40	50.43	-0.40

527 or double bounce scattering (Z4) near the Dhundi base is prominent even during the winter  
 528 (Figure 4.1(a)). So, this could effectively reduce the volume and surface coherences (section  
 529 2.2) thereby explaining this observation.

## 530 5. Conclusion and Future Scope

531 The primary focus of this research lies in estimating the SSD using the improved  
 532 hybrid DEM differencing and coherence amplitude inversion algorithm based on the single-  
 533 baseline Pol-InSAR technique (section 2.2). A time series analysis of the SSD estimates  
 534 involving six TSX/TDX datasets acquired between December 2015 and January 2016 have  
 535 been performed. Accordingly, the corresponding SSWEs are obtained by multiplying fixed  
 536 standing snow densities for each epoch.

537 Due to the complex hydrometeorological and topographical conditions of the study  
 538 area (section 3.1.1), significant uncertainty sources are present. These include the forests,  
 539 boulders, highly rough surfaces, and human settlements (Figure 3.2) which substantially  
 540 reduce the surface and volume scattering coherences required to estimate the snow depths  
 541 with adequate accuracy (section 2.3). Moreover, the limited ground-truth data availability  
 542 has always been a major challenge from the onset of this work (section 3.2). Apart from this,  
 543 the SAR data are affected by layover, shadowing and foreshortening in mountainous terrains  
 544 and hence, these errors are inherently propagated through the subsequent processing steps.  
 545 Furthermore, the Pol-InSAR model involves several user-defined parameters which have to  
 546 be optimised (section 2). In short, these are the main concerns involved in this work which  
 547 are addressed by means of identifying the potential uncertainty sources ( $H/\alpha$  decomposition  
 548 and Wishart classification) and performing appropriate sensitivity analysis (section 2.3.3).

549 Thus, the novelty of this research lies in suitably modifying and ultimately improving the  
 550 hybrid Pol-InSAR model (section 2.2) to estimate the SSD which is new in the context of  
 551 cryospheric studies. Although there was only a single spatial validation point (Dhundi), the  
 552 SSD estimates show high accuracy when the temporal trends are considered. Intriguingly,  
 553 only one of the free parameters,  $\eta'$ , needed to be tweaked for the time series analysis.  
 554 Therefore, the results suggest that the SSD inversion model works sufficiently well under  
 555 the complex hydrometeorological situations.

556 As part of future work, it is recommended to use the multi-baseline Pol-InSAR technique  
 557 (Cloude, 2010) wherein  $k_z$  can be simulated (instead of scaling by  $\eta'$ ) after an appropriate

558 accuracy assessment (Kumar et al., 2017). Similarly, the effect of different window shapes  
559 (square or rectangular) and sizes can be considered for the ensemble averaging operation.  
560 This sort of sensitivity analysis will help in deciding optimal window structures. Moreover, it  
561 is recommended to apply scattering mechanism based masks in conjunction with snow masks  
562 prepared from the high resolution optical datasets such as those provided by Sentinel-2 (Zhu  
563 et al., 2015). In addition, the prior classification of the dry and wet snow including the  
564 preparation of snow cover maps (Leinss et al., 2018; Thakur et al., 2012; Zhu et al., 2015)  
565 as necessary preprocessing steps will certainly improve the uncertainty assessment process.

566 Also, the use of the newer multi-temporal high resolution L-band datasets acquired by  
567 the upcoming SAR missions (Tridon et al., 2018; Rosen et al., 2017) is recommended to  
568 further verify and validate these models. Moreover, radar altimeters such as the Ka-band  
569 InSAR altimeter could potentially improve the SD and SWE estimates, and could also be  
570 used for operational snow depth monitoring on a large-scale (Hensley et al., 2016; Kim et al.,  
571 2018; Moller et al., 2011; Speziali et al., 2018).

572 In this work, only six datasets were used for analysis. Preferably, if a full scale time  
573 series analysis involving several epochs and multiple validation sites is performed, then the  
574 robustness of the SSD retrieval model can be even appropriately verified. Furthermore, Pol-  
575 InSAR coherency optimisation can be carried out to suitably adjust the scattering phase  
576 centres (Cloude, 2005, 2010). Moreover, the snow densities need to be computed gridwise  
577 (or if possible, pixelwise) by using hydrological modelling approaches (Bartelt & Lehning,  
578 2002; Liang et al., 1994). These can also be estimated from the PolSAR based techniques  
579 which are in practice (Singh et al., 2017; Thakur et al., 2012). Finally, necessary statistical  
580 hypothesis testing is required to suitably quantify the uncertainties associated with the SSD  
581 and SSWE estimates.

## 582 Acknowledgements

583 This research work was carried out as part of the ISRO EOAM mountain ecosystem,  
584 TANDEM-X AO and ALOS-RA4 project (EOAM-ME (WRD)) on the Himalayan glaciers.  
585 Also, this work was conducted within the IIRS, ISRO and University of Twente, Faculty  
586 ITC joint education programme (JEP) framework. The authors are grateful to IIRS, ISRO,  
587 University of Twente, Faculty ITC along with SASE, DRDO and the entire opensource  
588 community for providing the necessary means to conduct this study.

## 589 References

- 590 Abe, T., Yamaguchi, Y., & Sengoku, M. (1990). Experimental study of microwave transmission in snowpack.  
591 *IEEE Trans. Geosci. Remote Sens.*, 28, 915–921. doi:10.1109/36.58981.
- 592 Balss, U., Breit, H., Duque, S., Fritz, T., & Rossi, C. (2012). *CoSSC Generation and Interferometric*  
593 *Considerations (TD-PGS-TN-3129)*. Technical Report Remote Sensing Technology Institute,  
594 DLR Oberpfaffenhofen, Germany. URL: [https://tandemx-science.dlr.de/pdfs/TD-PGS-TN-3129\\_](https://tandemx-science.dlr.de/pdfs/TD-PGS-TN-3129_CoSSCGenerationInterferometricConsiderations_1.0.pdf)  
595 [CoSSCGenerationInterferometricConsiderations\\_1.0.pdf](https://tandemx-science.dlr.de/pdfs/TD-PGS-TN-3129_CoSSCGenerationInterferometricConsiderations_1.0.pdf).
- 596 Bartelt, P., & Lehning, M. (2002). A physical SNOWPACK model for the Swiss avalanche warning. *Cold*  
597 *Reg. Sci. Technol.*, 35, 123–145. doi:10.1016/S0165-232X(02)00074-5.

- 598 Brunner, D. (2009). *Advanced Methods For Building Information Extraction From Very High Resolution*  
599 *SAR Data To Support Emergency Response*. Doctoral thesis Trento: University of Trento. URL: [http://eprints-phd.biblio.unitn.it/233/1/PHD\\_Thesis\\_Dominik\\_Brunner.pdf](http://eprints-phd.biblio.unitn.it/233/1/PHD_Thesis_Dominik_Brunner.pdf).  
600
- 601 Cheney, E. W., & Kincaid, D. R. (2012). Nonlinear equations. In *Numer. Math. Comput.* (pp. 114–150).  
602 Boston, USA: Cengage Learning. (7th ed.).
- 603 Cloude, S. R. (2005). *POL-InSAR training course*. Technical Report ESA. URL: [https://earth.esa.int/landtraining07/pol-insar\\_training\\_course.pdf](https://earth.esa.int/landtraining07/pol-insar_training_course.pdf).  
604
- 605 Cloude, S. R. (2010). *Polarisation: Applications in Remote Sensing*. New York: Oxford University Press.  
606 doi:10.1093/acprof:oso/9780199569731.001.0001.
- 607 Conde, V., Nico, G., Mateus, P., Catalão, J., Kontu, A., & Gritsevich, M. (2019). On The Estimation of  
608 Temporal Changes of Snow Water Equivalent by Spaceborne Sar Interferometry: A New Application for  
609 the Sentinel-1 Mission. *J. Hydrol. Hydromechanics*, 67. doi:10.2478/johh-2018-0003.
- 610 Deems, J. S., Painter, T. H., & Finnegan, D. C. (2013). Lidar measurement of snow depth: a review. *J.*  
611 *Glaciol.*, 59, 467–479. doi:10.3189/2013JoG12J154.
- 612 ESA (2019). SNAP. URL: <http://step.esa.int/main/toolboxes/snap/>.
- 613 Guneriusson, T., Høgda, K. A., Johnsen, H., & Lauknes, I. (2001). InSAR for estimation of changes in snow  
614 water equivalent of dry snow. *IEEE Trans. Geosci. Remote Sens.*, 39, 2101–2108. doi:10.1109/36.957273.
- 615 Hajnsek, I., Kugler, F., Lee, S.-K., & Papathanassiou, K. P. (2009). Tropical-Forest-Parameter Estimation  
616 by Means of Pol-InSAR: The INDREX-II Campaign. *IEEE Trans. Geosci. Remote Sens.*, 47, 481–493.  
617 doi:10.1109/TGRS.2008.2009437.
- 618 Hanssen, R. F. (2001). *Radar Interferometry - Data Interpretation and Error Analysis* volume 2 of  
619 *Remote Sensing and Digital Image Processing*. Dordrecht: Kluwer Academic Publishers. doi:10.1007/  
620 0-306-47633-9.
- 621 Hensley, S., Moller, D., Oveisgharan, S., Michel, T., & Wu, X. (2016). Ka-Band Mapping and Measurements  
622 of Interferometric Penetration of the Greenland Ice Sheets by the GLISTIN Radar. *IEEE J. Sel. Top.*  
623 *Appl. Earth Obs. Remote Sens.*, 9, 2436–2450. doi:10.1109/JSTARS.2016.2560626.
- 624 Hoen, E. W., & Zebker, H. (2000). Penetration depths inferred from interferometric volume decorrelation  
625 observed over the Greenland Ice Sheet. *IEEE Trans. Geosci. Remote Sens.*, 38, 2571–2583. doi:10.1109/  
626 36.885204.
- 627 JetBrains (2020). PyCharm Documentation. URL: [https://www.jetbrains.com/pycharm/  
628 documentation/index.html](https://www.jetbrains.com/pycharm/documentation/index.html).
- 629 Jones, E., Oliphant, E., & Peterson, P. (2001). SciPy: Open Source Scientific Tools for Python. URL:  
630 <http://www.scipy.org/>.
- 631 Kim, E. J., Gatebe, C. K., Hall, D. K., & Kang, D. H. (2018). *NASA's SnowEx Campaign and Measuring*  
632 *Global Snow from Space (GSFC-E-DAA-TN55784)*. Technical Report NASA Pyeongchang, Republic of  
633 Korea. URL: <https://ntrs.nasa.gov/search.jsp?R=20180005187>.
- 634 Kugler, F., Lee, S.-K., Hajnsek, I., & Papathanassiou, K. P. (2015). Forest Height Estimation by Means of  
635 Pol-InSAR Data Inversion: The Role of the Vertical Wavenumber. *IEEE Trans. Geosci. Remote Sens.*,  
636 53, 5294–5311. doi:10.1109/TGRS.2015.2420996.
- 637 Kumar, S., Khati, U. G., Chandola, S., Agrawal, S., & Kushwaha, S. P. (2017). Polarimetric SAR  
638 Interferometry based modeling for tree height and aboveground biomass retrieval in a tropical deciduous  
639 forest. *Adv. Sp. Res.*, 60, 571–586. doi:10.1016/j.asr.2017.04.018.

- 640 Lee, J.-S., & Pottier, E. (2009). *Polarimetric Radar Imaging: From Basics to Applications*. Boca Raton,  
641 Florida, USA: CRC Press. URL: <https://www.taylorfrancis.com/books/9781420054972>.
- 642 Lee, J.-S., Schuler, D. L., & Ainsworth, T. L. (2000). Polarimetric SAR data compensation for terrain  
643 azimuth slope variation. *IEEE Trans. Geosci. Remote Sens.*, *38*, 2153–2163. doi:10.1109/36.868874.
- 644 Leica Geosystems AG (2012). *Leica GS10/GS15 User Manual (772916-4.1.0en)*. Technical Report Leica  
645 Geosystems AG Heerbrugg, Switzerland. URL: [http://www.surveyequipment.com/PDFs/Leica\\_Viva\\_GS10\\_GS15\\_User\\_Manual.pdf](http://www.surveyequipment.com/PDFs/Leica_Viva_GS10_GS15_User_Manual.pdf).  
646
- 647 Leinss, S., Antropov, O., Vehvilainen, J., Lemmetyinen, J., Hajnsek, I., & Praks, J. (2018). Wet Snow Depth  
648 from Tandem-X Single-Pass Insar Dem Differencing. In *IGARSS 2018 - 2018 IEEE Int. Geosci. Remote*  
649 *Sens. Symp.* (pp. 8500–8503). IEEE. doi:10.1109/IGARSS.2018.8518661.
- 650 Leinss, S., Löwe, H., Proksch, M., Lemmetyinen, J., Wiesmann, A., & Hajnsek, I. (2016). Anisotropy  
651 of seasonal snow measured by polarimetric phase differences in radar time series. *The Cryosphere*, *10*,  
652 1771–1797. doi:10.5194/tc-10-1771-2016.
- 653 Leinss, S., Parrella, G., & Hajnsek, I. (2014). Snow height determination by polarimetric phase differences  
654 in X-Band SAR Data. *IEEE J. Sel. Top. Appl. Earth Obs. Remote Sens.*, *7*, 3794–3810. doi:10.1109/  
655 *JSTARS*.2014.2323199.
- 656 Leinss, S., Wiesmann, A., Lemmetyinen, J., & Hajnsek, I. (2015). Snow Water Equivalent of Dry Snow  
657 Measured by Differential Interferometry. *IEEE J. Sel. Top. Appl. Earth Obs. Remote Sens.*, *8*, 3773–  
658 3790. doi:10.1109/JSTARS.2015.2432031.
- 659 Li, H., Wang, Z., He, G., & Man, W. (2017). Estimating Snow Depth and Snow Water Equivalence Using  
660 Repeat-Pass Interferometric SAR in the Northern Piedmont Region of the Tianshan Mountains. *J.*  
661 *Sensors*, *2017*, 1–17. doi:10.1155/2017/8739598.
- 662 Liang, X., Lettenmaier, D. P., Wood, E. F., & Burges, S. J. (1994). A simple hydrologically based model of  
663 land surface water and energy fluxes for general circulation models. *J. Geophys. Res.*, *99*, 14415–14428.  
664 doi:10.1029/94JD00483.
- 665 Liu, Y., Li, L., Yang, J., Chen, X., & Hao, J. (2017). Estimating snow depth using multi-source data fusion  
666 based on the D-InSAR method and 3DVAR fusion algorithm. *Remote Sens.*, *9*. doi:10.3390/rs9111195.
- 667 Luo, X., Richter, B., & Cole, A. (2014). *GLONASS only and BeiDou only RTK Positioning*. Technical Report  
668 Leica Geosystems AG Heerbrugg, Switzerland. URL: [https://leica-geosystems.com/-/media/Files/LeicaGeosystems/Products/WhitePapers/GLONASS\\_BeiDou\\_RTK\\_Positioning\\_WPA.ashx](https://leica-geosystems.com/-/media/Files/LeicaGeosystems/Products/WhitePapers/GLONASS_BeiDou_RTK_Positioning_WPA.ashx).  
669
- 670 Majumdar, S., Thakur, P. K., Chang, L., & Kumar, S. (2019a). X-Band Polarimetric SAR Copolar Phase  
671 Difference for Fresh Snow Depth Estimation in the Northwestern Himalayan Watershed. In *IGARSS 2019*  
672 *- 2019 IEEE Int. Geosci. Remote Sens. Symp.* (pp. 4102–4105). Yokohama, Japan. doi:10.1109/IGARSS.  
673 *2019*.8898884.
- 674 Majumdar, S., Thakur, P. K., Chang, L., Kumar, S., & Smith, R. (2019b). Spaceborne Polarimetric SAR  
675 Interferometry for Snow Depth Retrieval in the Northwestern Himalayan Watershed. In *Geol. Soc. Am.*  
676 *Abstr. with Programs*. Phoenix, AZ, USA. doi:10.1130/abs/2019AM-338916.
- 677 Moller, D., Hensley, S., Sadowy, G. A., Fisher, C. D., Michel, T., Zawadzki, M., & Rignot, E. (2011). The  
678 Glacier and Land Ice Surface Topography Interferometer: An Airborne Proof-of-Concept Demonstration  
679 of High-Precision Ka-Band Single-Pass Elevation Mapping. *IEEE Trans. Geosci. Remote Sens.*, *49*, 827–  
680 842. doi:10.1109/TGRS.2010.2057254.

- 681 Moreira, A., Prats-Iraola, P., Younis, M., Krieger, G., Hajnsek, I., & Papathanassiou, K. P. (2013). A  
682 tutorial on synthetic aperture radar. *IEEE Geosci. Remote Sens. Mag.*, 1, 6–43. doi:10.1109/MGRS.  
683 2013.2248301.
- 684 Papathanassiou, K., & Cloude, S. (2001). Single-baseline polarimetric SAR interferometry. *IEEE Trans.*  
685 *Geosci. Remote Sens.*, 39, 2352–2363. doi:10.1109/36.964971.
- 686 QGIS Development Team (2019). QGIS Geographic Information System. URL: <http://qgis.osgeo.org/>.
- 687 Reynolds, B. (1983). The chemical composition of snow at a rural upland site in Mid-wales. *Atmos. Environ.*,  
688 17, 1849–1851. doi:10.1016/0004-6981(83)90193-2.
- 689 Riche, F., Montagnat, M., & Schneebeli, M. (2013). Evolution of crystal orientation in snow during  
690 temperature gradient metamorphism. *J. Glaciol.*, 59, 47–55. doi:10.3189/2013JG12J116.
- 691 Rosen, P., Hensley, S., Shaffer, S., Edelstein, W., Kim, Y., Kumar, R., Misra, T., Bhan, R., & Sagi, R.  
692 (2017). The NASA-ISRO SAR (NISAR) mission dual-band radar instrument preliminary design. In 2017  
693 *IEEE Int. Geosci. Remote Sens. Symp.* (pp. 3832–3835). IEEE. doi:10.1109/IGARSS.2017.8127836.
- 694 Sharma, J., Hajnsek, I., & Papathanassiou, K. (2007). Multi-frequency polinsar signatures of a subpolar  
695 glacier. In *International Workshop on Applications of Polarimetry and Polarimetric Interferometry (Pol-*  
696 *InSAR)* (p. 8). URL: <https://elib.dlr.de/47426/>.
- 697 Singh, G., Venkataraman, G., Yamaguchi, Y., & Park, S.-E. (2014). Capability Assessment of Fully  
698 Polarimetric ALOSPALSAR Data for Discriminating Wet Snow From Other Scattering Types in  
699 Mountainous Regions. *IEEE Trans. Geosci. Remote Sens.*, 52, 1177–1196. doi:10.1109/TGRS.2013.  
700 2248369.
- 701 Singh, G., Verma, A., Kumar, S., Snehmani, Ganju, A., Yamaguchi, Y., & Kulkarni, A. V. (2017). Snowpack  
702 Density Retrieval Using Fully Polarimetric TerraSAR-X Data in the Himalayas. *IEEE Trans. Geosci.*  
703 *Remote Sens.*, 55, 6320–6329. doi:10.1109/TGRS.2017.2725979.
- 704 Snehmani, Venkataraman, G., Nigam, A. K., & Singh, G. (2010). Development of an inversion algorithm for  
705 dry snow density estimation and its application with ENVISAT-ASAR dual co-polarization data. *Geocarto*  
706 *Int.*, 25, 597–616. doi:10.1080/10106049.2010.516843.
- 707 Speziali, F., Trampuz, C., Placidi, S., Hendriks, L. C. I., Ludwig, M., & Meta, A. (2018). Development of  
708 the Multichannel Interferometric Ka-Band Airborne SAR Instrument (KaSAR). In *EUSAR 2018; 12th*  
709 *Eur. Conf. Synth. Aperture Radar* (pp. 1–5). Aachen, Germany. URL: [https://ieeexplore.ieee.org/  
710 abstract/document/8438262](https://ieeexplore.ieee.org/abstract/document/8438262).
- 711 Takala, M., Luoju, K., Pulliainen, J., Derksen, C., Lemmetyinen, J., Kärnä, J.-P., Koskinen, J., & Bojkov,  
712 B. (2011). Estimating northern hemisphere snow water equivalent for climate research through assimilation  
713 of space-borne radiometer data and ground-based measurements. *Remote Sens. Environ.*, 115, 3517–3529.  
714 doi:10.1016/j.rse.2011.08.014.
- 715 Tedesco, M. (Ed.) (2015). *Remote Sensing of the Cryosphere*. Chichester, UK: John Wiley & Sons, Ltd.  
716 doi:10.1002/9781118368909.
- 717 Thakur, P. K., Aggarwal, S., Garg, P., Garg, R., Mani, S., Pandit, A., & Kumar, S. (2012). Snow physical  
718 parameters estimation using space-based Synthetic Aperture Radar. *Geocarto Int.*, 27, 263–288. doi:10.  
719 1080/10106049.2012.672477.
- 720 Thakur, P. K., Aggarwal, S. P., Arun, G., Sood, S., Senthil Kumar, A., Mani, S., & Dobhal, D. P.  
721 (2017). Estimation of Snow Cover Area, Snow Physical Properties and Glacier Classification in  
722 Parts of Western Himalayas Using C-Band SAR Data. *J. Indian Soc. Remote Sens.*, 45, 525–539.  
723 doi:10.1007/s12524-016-0609-y.

- 724 Tridon, D. B., Sica, F., De Zan, F., Bachmann, M., & Krieger, G. (2018). Observation Strategy and Flight  
725 Configuration for Monitoring Earth Dynamics with the Tandem-L Mission. In *IGARSS 2018 - 2018 IEEE*  
726 *International Geoscience and Remote Sensing Symposium* (pp. 5651–5654). doi:[10.1109/IGARSS.2018.](https://doi.org/10.1109/IGARSS.2018.8517757)  
727 [8517757](https://doi.org/10.1109/IGARSS.2018.8517757).
- 728 Ulaby, F., Stiles, W., Dellwig, L., & Hanson, B. (1977). Experiments on the Radar Backscatter of Snow.  
729 *IEEE Trans. Geosci. Electron.*, *15*, 185–189. doi:[10.1109/TGE.1977.294490](https://doi.org/10.1109/TGE.1977.294490).
- 730 Usami, N., Muhuri, A., Bhattacharya, A., & Hirose, A. (2016). PolSAR Wet Snow Mapping With Incidence  
731 Angle Information. *IEEE Geosci. Remote Sens. Lett.*, *13*, 2029–2033. doi:[10.1109/LGRS.2016.2621891](https://doi.org/10.1109/LGRS.2016.2621891).
- 732 Wu, S., Li, J., & Huang, G. H. (2008). A study on DEM-derived primary topographic attributes for hydrologic  
733 applications: Sensitivity to elevation data resolution. *Appl. Geogr.*, *28*, 210–223. doi:[10.1016/j.apgeog.](https://doi.org/10.1016/j.apgeog.2008.02.006)  
734 [2008.02.006](https://doi.org/10.1016/j.apgeog.2008.02.006).
- 735 Yueh, S., Dinardo, S., Akgiray, A., West, R., Cline, D., & Elder, K. (2009). Airborne Ku-Band Polarimetric  
736 Radar Remote Sensing of Terrestrial Snow Cover. *IEEE Trans. Geosci. Remote Sens.*, *47*, 3347–3364.  
737 doi:[10.1109/TGRS.2009.2022945](https://doi.org/10.1109/TGRS.2009.2022945).
- 738 Zhu, Z., Wang, S., & Woodcock, C. E. (2015). Improvement and expansion of the Fmask algorithm: cloud,  
739 cloud shadow, and snow detection for Landsats 47, 8, and Sentinel 2 images. *Remote Sens. Environ.*, *159*,  
740 269–277. doi:[10.1016/j.rse.2014.12.014](https://doi.org/10.1016/j.rse.2014.12.014).
- 741 Zuniga, M., Habashy, T., & Kong, J. (1979). Active Remote Sensing of Layered Random Media. *IEEE*  
742 *Trans. Geosci. Electron.*, *17*, 296–302. doi:[10.1109/TGE.1979.294658](https://doi.org/10.1109/TGE.1979.294658).